



HAL
open science

Sunflower Hydrogenation in Taylor Flow Conditions: Experiments and Computational Fluid Dynamics Modeling Using a Moving Mesh Approach

Pierre Albrand, Carine Julcour-Lebigue, Anne-Marie Billet

► **To cite this version:**

Pierre Albrand, Carine Julcour-Lebigue, Anne-Marie Billet. Sunflower Hydrogenation in Taylor Flow Conditions: Experiments and Computational Fluid Dynamics Modeling Using a Moving Mesh Approach. *Industrial & Engineering Chemistry Research*, 2021, 60 (46), pp.16701-16719. 10.1021/acs.iecr.1c02801 . hal-03589181

HAL Id: hal-03589181

<https://hal.science/hal-03589181>

Submitted on 25 Feb 2022

HAL is a multi-disciplinary open access archive for the deposit and dissemination of scientific research documents, whether they are published or not. The documents may come from teaching and research institutions in France or abroad, or from public or private research centers.

L'archive ouverte pluridisciplinaire **HAL**, est destinée au dépôt et à la diffusion de documents scientifiques de niveau recherche, publiés ou non, émanant des établissements d'enseignement et de recherche français ou étrangers, des laboratoires publics ou privés.



Open Archive Toulouse Archive Ouverte (OATAO)

OATAO is an open access repository that collects the work of Toulouse researchers and makes it freely available over the web where possible

This is an author's version published in: <http://oatao.univ-toulouse.fr/28569>

Official URL: <https://doi.org/10.1021/acs.iecr.1c02801>

To cite this version:

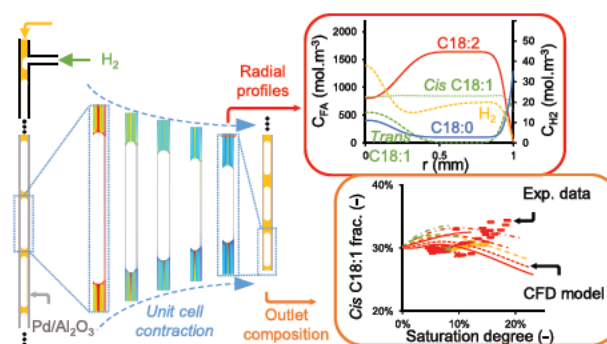
Albrand, Pierre  and Julcour-Lebigue, Carine  and Billet, Anne-Marie 
Sunflower Hydrogenation in Taylor Flow Conditions: Experiments and Computational Fluid Dynamics Modeling Using a Moving Mesh Approach.
(2021) *Industrial & Engineering Chemistry Research*, 60 (46). 16701-16719.
ISSN 1520-5045

Any correspondence concerning this service should be sent
to the repository administrator: tech-oatao@listes-diff.inp-toulouse.fr

Sunflower Hydrogenation in Taylor Flow Conditions: Experiments and Computational Fluid Dynamics Modeling Using a Moving Mesh Approach

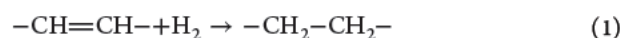
Pierre Albrand,* Carine Julcour,* and Anne-Marie Billet*

ABSTRACT: Sunflower oil hydrogenation was carried out in a 2 mm diameter jacketed capillary reactor coated with a Pd/Al₂O₃ catalyst, mimicking a channel of a heat exchanger monolith reactor. The operating conditions were chosen to ensure Taylor flow conditions and to evaluate their impact on the reaction selectivity. CFD simulations of the experiments were performed using the unit cell approach. They accounted for the dependence of viscosity on the degree of oil saturation, kinetic laws describing the effects of pressure on *cis/trans* selectivity, and bubble shrinkage along the channel using a moving mesh strategy. The model captured the experimental trends, in which the fraction of monounsaturated *cis* fatty acids did not exceed 35% (vs 30% originally). Poor selectivity is mainly due to the strong mass transfer resistance at the catalyst wall, either from fatty acids (favoring their complete saturation) and/or from hydrogen (due to bubble shrinkage, favoring *cis* to *trans* isomerization).



INTRODUCTION

Hydrogenation of edible oils consists of transforming the carbon–carbon double bonds (or *unsaturations*) present in fatty acids into single bonds, by reaction with hydrogen in the presence of a solid catalyst, as shown by eq 1.



This process is widely used in food and cosmetic industries to increase viscosity, hence texture, while reducing the oil rancidity.^{1,2} Along with saturation reactions, isomerization reactions can also take place where naturally present *cis* unsaturations are turned into *trans* unsaturations (Figure 1).

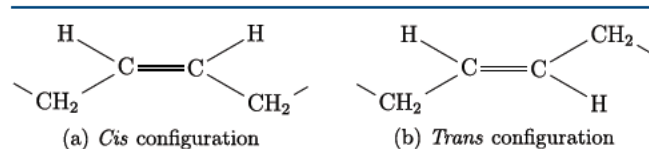


Figure 1. Configurations of carbon–carbon double bonds (*unsaturations*) in unsaturated fatty acids: *cis* (a) and *trans* (b) isomers.

The *trans* fatty acids (TFA) and to some extent fully saturated fatty acids (SFA) are known to be harmful to human health since their dietary consumption can lead to cardiovascular diseases, such as atherosclerosis.^{3,4}

In this context, the hydrogenation process aims to be particularly selective: monounsaturated fatty acids (MUFA) with a remaining *cis* unsaturation have to be favored. Thus,

hydrogenation of polyunsaturated fatty acids (PUFA) should prevail, while limiting as much as possible *cis* to *trans* isomerization reactions.

At the industrial scale, edible oil hydrogenation is traditionally carried out in batch dead end reactor with a slurry of nickel (Ni) based catalyst.⁵ This metal exhibits poor selectivity toward TFA and MUFA.⁶ Furthermore, operating conditions used in large reactors (low pressure, high temperature) and limited gas–liquid mass transfer favor TFA production.^{5,7}

As a consequence, extensive work has been done concerning innovative reactors which could possibly improve the selectivity of edible oil hydrogenation. For instance, Veldsink⁸ and Fritsch and Bengtson⁹ used membranes impregnated with Pd and Pt, respectively, for sunflower oil hydrogenation. In both cases, TFA production was equivalent to that encountered in slurry reactors.

Remarkable results were achieved by Macher et al.¹⁰ who used fatty acid methyl esters from rapeseed oil diluted in propane. They managed to reach 3.8% TFA for an iodine value (IV) of 70 by employing a trickle bed reactor with Pd impregnated pellets.

Boger et al.¹¹ and Boldrini et al.¹² studied the hydrogenation of soybean and sunflower oils, respectively, in a monolith stirred

reactor. In both cases, monolith blocks were attached to the impeller, and a catalyst was deposited at the channels wall (washcoat). The first authors compared this setup performance with slurry hydrogenation. The monolith stirred reactor slightly improved TFA and MUFA compositions for IV lower than 90.

As a consequence, innovative three phase monolith type reactors have grown in interest in recent years, due to the particular features of the Taylor flow where bubbles are separated by liquid slugs.^{13–15} Such a flow structure indeed provides plug flow behavior and a low pressure drop, while enhancing gas–liquid mass transfer due to the presence of recirculation vortices in the liquid slugs and a thin lubrication film between the bubbles and the wall.¹⁶

The Taylor flow hydrodynamic features have been the subject of several reviews.^{17–19} In brief, it is characterized by a predominance of capillary effects over gravitational, viscous, or inertial effects, which results in the following dimensionless numbers being most often less than unity:

- Capillary number (ratio between viscous and surface tension forces): $Ca = \mu_L U_B / \sigma_L$
- Weber number (ratio between inertial and surface tension forces): $We = \rho_L U_B^2 d_c / \sigma_L$
- Bond number (ratio between gravitational and surface tension forces): $Bo = (\rho_L - \rho_G) g d_c^2 / \sigma_L$

values of Bo between 0.88 and $(2\pi)^2$ were proposed to delineate the diameter range for “small channels” or “capillaries”.^{20,21}

In addition, the flow regime is usually laminar in the liquid slug, with a Reynolds number based on the bubble velocity, $Re = \rho_L U_B d_c / \mu_L$, less than 1000, for instance, $0.01 < Ca < 0.1$ and $Re < 200$ in Woo and co workers^{14,15} and $Ca < 0.01$ and $Re < 1000$ in Durán Martínez.¹³ Ca and Re values usually determine liquid film thickness, slug length, bubble shape, or two phase pressure drop.²²

In a previous contribution,²³ a simulation strategy of a heat exchanger monolith reactor was developed for sunflower oil hydrogenation. It described the strong multiphysics coupling between hydrodynamics, transport phenomena (mass transfer), and reaction in the channels, due to the evolution of viscosity and diffusivity during the oil hydrogenation. This CFD study highlighted important mass transfer resistance for fatty acids, transported as triglyceride (TAG) molecules. The consequence of this phenomenon is that the freshly produced MUFA from PUFA hydrogenation at the channel wall were saturated in turn. It also showed that the increase in oil viscosity during the reaction had to be taken into account to avoid significant undersizing of the reactor.

Nevertheless, this study had a couple of shortcomings. There was no distinction between *cis* and *trans* MUFA, as well as no consideration of the bubbles size reduction due to gas consumption along the channel. Furthermore, an experimental proof of concept was lacking.

The present work aims to deal with these specific issues. A newly developed kinetic model proposed by Albrand et al.,²⁴ which introduces a distinct dependency to operating conditions for saturation and isomerization reactions, is considered here. Moreover, an original moving mesh approach is able to take into account the bubble reduction and, hence, the evolution of the gas–liquid surface area along the channel.

Numerical results are compared with those from hydrogenation experiments carried out in a single channel reactor. This single channel configuration allows for precise control of

gas and liquid flows at the inlet and avoids the fluid maldistribution often reported in monolith reactors.^{25,26}

Finally, mass transfer coefficients are calculated from the CFD simulations and compared with existing correlations.

■ EXPERIMENTAL STUDY OF SUNFLOWER OIL HYDROGENATION IN SINGLE CHANNEL REACTOR

Materials and Methods. *Description of Experimental Setup.* The sunflower oil was supplied by ITERG (Pessac, France), and its composition before hydrogenation is available in the [Supporting Information](#) (Table S1).

The hydrogenation pilot unit used in this study consists of a single channel reactor operating in Taylor flow conditions. It comprises four *monotubes* assembled vertically in series as shown in [Figure 2](#).

These jacketed tubes have been manufactured by the society FusiA AeroAdditive (Toulouse, France) using laser fusion of a AlSi10Mg alloy. Each monotube is 20 cm long and has a 2 mm internal diameter ([Figure 3](#)). Two of them are used as received, while the other two contain a catalytic *washcoat* deposited on their internal wall. This washcoat is made of porous γ -Al₂O₃ alumina impregnated with palladium (Pd). It has been synthesized by the society Mecaprotec Industries (Muret, France), according to a similar procedure¹³ as applied for the Pd/Al₂O₃ powder used for the kinetic study,²⁴ with a Pd content of 0.7 wt %. Its thickness, δ_c , is between 7.5 and 15 μm ;¹³ it is also of the same order of magnitude as the characteristic diffusion length in the powdered catalyst.

The vegetable oil is kept in a stirred heated stainless steel tank and fed to the in series monotubes by a HPLC pump (Multitherm 200 3351, Bischoff Chromatography), equipped with a heated head. The liquid circuit is traced with a heating cord. The edible oil enters at the top of the first uncoated monotube ([Figure 2](#)), which acts as a preheater. Thermal oil, whose temperature is controlled by a heat transfer unit (Lauda ITH 150), circulates upward in the jacket of the tubes, which are maintained between insulating plates. Hydrogen (Air Liquide, purity of 99.95%) is introduced in the second uncoated monotube by means of a T junction. It allows gas–liquid saturation prior to the catalytic section. The gas flow rate is regulated by a flow controller (Brooks SLAS860S). Pressure is measured at the inlet of the first tube (Keller transducer, 0–100 bar), and its value is set using a backpressure regulator placed at the gas outlet. Pt100 temperature probes are located at the inlet and outlet of each monotube.

After reaction in the two catalytic monotubes, the partially hydrogenated oil and the hydrogen are disengaged in a gas–liquid separator, where the liquid is collected, and the gas is ultimately sent to the vent after being dried, filtered, and diluted with N₂.

Experimental Procedure and Samples Analysis. Once the two catalytic monotubes were assembled on the pilot unit, *in situ* activation of the catalyst was carried out under hydrogen flow, for 30 min at 100 °C, then 90 min at 230 °C (with successively downward and upward flow).

After the activation was completed, the heat transfer system was switched on to heat the reactor at the predefined temperature (typically between 80 and 160 °C). The reactor was then pressurized (between 10 and 21 bar) by flowing hydrogen. Finally, the HPLC pump was turned on at the given liquid flow rate.

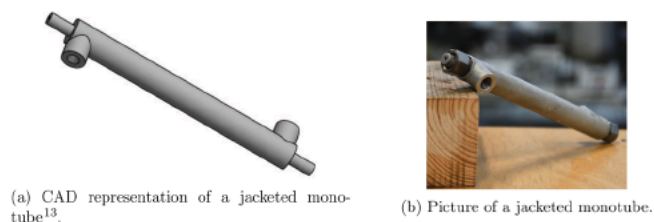
The entrance of the liquid in the first monotube was detected by a temperature drop of 2 °C. It was referred to as the zero time



Figure 2. Single channel hydrogenation unit.

of the experiment. Liquid samples (2 mL) were collected at the reactor outlet after about 3 min (10 times the theoretical residence time), then at given (increasing) time intervals (Figure 4).

Hydrogenated oil samples were characterized by gas chromatography with a flame ionization detection (GC/FID). They were first methylated with boron trifluoride, then injected



(a) CAD representation of a jacketed monotube¹³.

(b) Picture of a jacketed monotube.

Figure 3. Details of a monotube reactor: drawing (a) and photography (b).

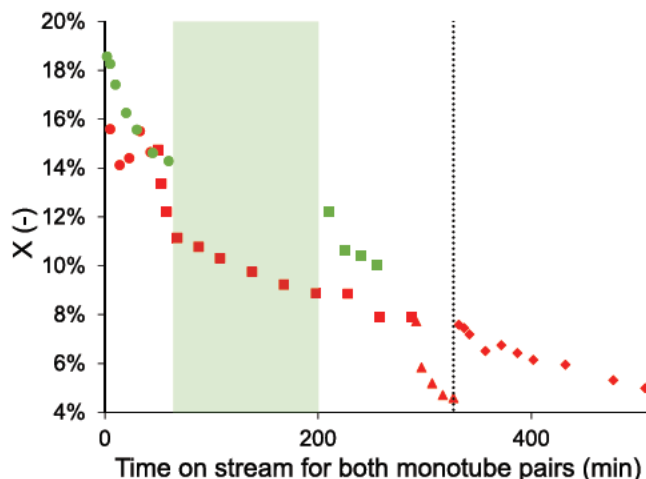


Figure 4. Evolution of the oil saturation degree at 160 °C and 21 bar for MT1 pair (red) and MT2 pair (green) as a function of the time on stream: MT1-C1-A1 and MT2-C3-A1 (●), MT1-C1-A2 and MT2-C3-A4 (■), MT1-C1-A3 (△), and MT1-C2-A1 (◇); cleaning and reduction under H₂ before MT1 C2 campaign (⋯).

into an Agilent FAME column (0.25 mm ID × 50 m, Agilent Select). An overall number of 21 fatty acids were identified on the chromatograph. However, only 18 carbon fatty acids were considered (representing more than 90 wt % of the oil). Additionally, with *trans* PUFA being in minority with respect to their *cis* counterparts, both isomers were counted as one C18:2 species.

Investigated Cases and Catalyst Activity Monitoring.
Experimental Campaigns. The reference conditions were set at 21 bar and 160 °C, respectively, to reach a high conversion level of the oil. This saturation degree of the partially hydrogenated oil, X , was calculated by eq 2, where p' is the average number of unsaturations per fatty acid present in the oil and p'_0 its value before hydrogenation.

$$X = \frac{p'_0 - p'}{p'_0} \quad (2)$$

Moreover, in order to achieve Taylor flow conditions, superficial velocities of gas (u_{GS}) and liquid (u_{LS}) had to be chosen carefully. While flow regime maps are available for air and water in capillary channels,²⁷ such two phase flow has not been investigated for hydrogen and vegetable oils to the authors' knowledge. Nevertheless, Taylor flow conditions should be met for both low u_{GS} and u_{LS} ²⁷ (here, <0.1 m/s). In addition, low superficial velocities ensured that the capillary number, Ca , remained low enough (below 10^{-2}) for the bubble shape to be still reasonably approximated as a cylinder with hemispherical caps at its ends,²⁸ even for such a highly viscous liquid.

Table 1. Operating Conditions of the Hydrogenation Experiments Carried out in Single Channel Reactor (Chronological Order)

Pair	Campaign	Assay	T ($^{\circ}\text{C}$)	P (bar)	$u_{LS,0}$ (m/s)	$u_{GS,0}$ (m/s)	$N_{samples}$ ()	t_{exp} (min)
Activation								
MT1	C1	A1	160	21	1.68×10^{-2}	4.63×10^{-2}	6	43
		A2	160	21	1.68×10^{-2}	4.63×10^{-2}	12	245
		A3	160	21	1.68×10^{-2}	4.63×10^{-2}	5	39
Cleaning and reactivation								
	C2	A1	160	21	1.68×10^{-2}	4.63×10^{-2}	10	180
Activation								
MT2	C3	A1	160	21	1.68×10^{-2}	4.63×10^{-2}	7	60
		A2	120	21	1.09×10^{-2}	2.48×10^{-2}	7	60
		A3	80	21	5.26×10^{-3}	1.35×10^{-2}	6	75
		A4	160	21	1.68×10^{-2}	4.63×10^{-2}	4	60
		A5	160	10	1.68×10^{-2}	5.73×10^{-2}	7	62

With H_2 being the limiting reactant as per the stoichiometry under the investigated conditions, a compromise had to be made regarding $u_{GS,0}/u_{LS,0}$ so as to maximize X , while avoiding annular flow; this inlet ratio was set between 2 and 3.5.

Two pairs of catalytic monotubes were used, MT1 and MT2, for an overall number of nine assays (two campaigns for MT1 and one for MT2). It is worth noting that the MT1 pair was cleaned with decane and reactivated between the two campaigns.

All assays and their respective operating conditions are given in Table 1, where $N_{samples}$ and t_{exp} are the number of samples taken during the experiment and the duration of the experiment, respectively. Hence, six out of the nine assays were carried out in the reference conditions (160 $^{\circ}\text{C}$, 21 bar) for comparison purposes. Lower temperatures (80 and 120 $^{\circ}\text{C}$) and pressure (10 bar) were also tested in order to evaluate potential effect on selectivity.²⁴ Moreover, flow rate conditions were changed as well, in order to increase residence time, since reaction rates were expected to be lower in these latter cases.

Catalyst Activity Evolution. For both the catalytic monotube pairs used in this work, Figure 4 depicts the saturation degree, X , measured at the reactor outlet during the repeated tests at 160 $^{\circ}\text{C}$ and 21 bar (as a function of the time on stream, i.e., the actual time of catalytic reactor operation). It is duly noted that the saturation degree never reaches a clear plateau during a given assay due to continuous catalyst deactivation. This observation differs from the behavior reported in the work of Boger et al.¹¹ who investigated the hydrogenation of edible oil catalyzed by palladium supported on monoliths. After three hydrogenation cycles, the authors reported a constant activity for the catalytic monolithic blocks mounted on a gas self inducing stirrer. This might be explained by the different reactor configuration, since their batchwise operation could have limited the catalyst exposition to impurities dissolved in the liquid load.

Both monotube pairs exhibited essentially the same activity trend: X dropped from 14.0% to 10.4% on average between MT1–C1–A1 and MT1–C1–A2 and from 16.4% to 10.8% between MT2–C3–A1 and MT2–C3–A4. This deactivation had thus to be accounted for in the modeling.

CFD MODELING OF SUNFLOWER OIL HYDROGENATION IN CAPILLARY CHANNEL USING A MOVING MESH APPROACH

Strategy. This section focuses on the CFD modeling of the previously described hydrogenation tests in a single channel

reactor operating in Taylor flow conditions. Numerical and experimental results aimed to be compared for model validation and process scale up following the overall strategy described by Albrand et al.²³ for heat exchanger reactors of monolith type.

Although hydrogenation is highly exothermic (-120 kJ mol^{-1}),⁷ efficient heat transfer at the wall of the capillary and high flow rate of the thermal oil in the jacket allow the single channel reactor to be considered as isothermal, as confirmed by the temperature measurements showing less than 1 $^{\circ}\text{C}$ increase along the monotubes. As mentioned above, inlet superficial velocities of gas and liquid were also chosen to ensure Taylor flow conditions, where the succession of bubbles and liquid slugs is known to enhance gas–liquid mass transfer.

The problem to solve involves coupled multiphysics phenomena: hydrodynamics, mass transport, and catalytic reactions. This coupling is even stronger in the case of edible oil hydrogenation, since the liquid viscosity, hence the diffusivity of the species, is changing with the saturation degree of the oil. It requires all the physics to be solved simultaneously. For this reason, COMSOL MULTIPHYSICS software has been chosen since it allows a straightforward coupling of these different phenomena and their description at the right level of complexity.

In addition, the bubbles shrink along the channel due to gas consumption, which can also affect the mass transfer performance due to a reduction of the gas–liquid interfacial area. This phenomenon has been also accounted for, thanks to a moving mesh strategy.

Modeling Framework. The unit cell (UC) approach is traditionally considered to simulate Taylor flow, since it takes advantage of the periodic pattern of this two phase flow.^{29,30} This strategy consists of setting a moving frame of reference centered on the bubble and comprising two half liquid slugs. Transient simulation of this unit cell reflects its motion along the channel and hence allows the simulation of the entire channel. This strategy is adequate for a fully developed flow, i.e., far from the inlet or outlet the channel. With the channel being cylindrical, a 2D axisymmetric domain is considered.

First, the “initial” unit cell geometry has to be defined that matches the investigated conditions. In the present case, superficial velocities of gas and liquid at the inlet, $u_{GS,0}$ and u_{LS} respectively, are known (Table 1). Inlet two phase and bubble velocities, $U_{TP,0}$ and $U_{B,0}$, are then deduced from eqs 3 and 4.³¹ Gas retention in the unit cell at the inlet, $\epsilon_{G,0}$, is finally calculated with eq 5.

Table 2. Inlet Properties, Velocities, and Gas Retention for Simulated Cases Deduced from Experimental Operating Conditions of Oil Hydrogenation Tests

Associated experiments	Case	T (°C)	P (bar)	$\mu_{L,0}$ (mPa s)	$\sigma_{L,0}$ (mN m ⁻¹)	$\rho_{L,0}$ (kg m ⁻³)	$U_{TP,0}$ (cm s ⁻¹)	$U_{B,0}$ (cm s ⁻¹)	$\epsilon_{G,0}$ (%)	Ca_0 ()
ref. conditions ^a	1	160	21	2.79	19.6	826	6.31	7.22	64.1	1.0×10^{-2}
MT2 C3 A2	2	120	21	4.85	23.6	853	3.56	3.99	62.0	8.2×10^{-3}
MT2 C3 A3	3	80	21	9.95	27.7	879	1.88	2.09	64.5	7.5×10^{-3}
MT2 C3 A5	4	160	10	2.79	19.6	826	7.41	8.63	66.4	1.2×10^{-2}

^aMT1–C1, MT1–C2, MT2–C3–A1, and MT2–C3–A4

$$U_{TP,0} = u_{GS,0} + u_{LS} \quad (3)$$

$$\frac{U_{B,0} - U_{TP,0}}{U_{B,0}} = 1.29 \times (3Ca_0)^{2/3} \quad (4)$$

$$u_{GS,0} = \epsilon_{G,0} U_{B,0} \quad (5)$$

Here, Ca_0 is the capillary number at the inlet and is equal to $\mu_{L,0} U_{B,0} / \sigma_{L,0}$, where $\mu_{L,0}$ and $\sigma_{L,0}$ are the dynamic viscosity and surface tension of the edible oil before hydrogenation, respectively. Predictions of physical properties are discussed later.

Preliminary calculations were subsequently made from experimental conditions available in Table 1. Results for the simulated cases associated with experimental assays are given in Table 2.

Ca_0 values range between 10^{-3} and 10^{-2} for all cases. The bubble should exhibit an “ideal” shape^{32,33} (i.e., a cylindrical body with two hemispheres at both ends) for capillary number close to or lower than 10^{-3} . On the other hand, using two phase flow simulations, Durán Martínez¹³ compared the overall gas–liquid mass flux calculated for “ideal” and “real” bubbles (corresponding to $Ca = 4 \times 10^{-3}$) and noted a 19% difference only. This difference is assumed to be small in regard to the effect of size reduction which is taking into account using a moving mesh approach. Consequently, the bubble shape is supposed to be ideal with a constant lubrication film thickness. δ_f is given by eq 6,³⁴ where R_C is the channel radius (1 mm, here).

$$\frac{\delta_f}{R_C} = \frac{1, 34Ca_0^{2/3}}{1 + 1.34(2.5)Ca_0^{2/3}} \quad (6)$$

The initial length of the unit cell, $L_{UC,0}$, cannot be estimated directly. Hence, its value is arbitrarily set to 40 mm, which lies within the typical order of magnitude.^{23,35} Another value was tested for Case 1: hereafter, Cases 1a and 1b stand for $L_{UC,0}$ equal to 40 and 20 mm, respectively.

At this point, the initial UC geometry can be fully obtained; the initial length of the lubrication film, $L_{f,0}$, is deduced from $L_{UC,0}$, $\epsilon_{G,0}$, and δ_f .

Liquid viscosity is large enough compared with that of the gas to neglect shear stress at the gas–liquid interface. From a hydrodynamic perspective, a slip boundary can simulate the interaction between the two phases.²³ Very low vapor pressure of the vegetable oil results in neglecting TAG mass transfer from the liquid phase to the gas phase.^{23,36} With the bubble content remaining pure hydrogen, only the liquid phase needs to be simulated.

As mentioned earlier, the channel is assumed to be isothermal. Pressure drop is also neglected.

Reactions in the catalytic washcoat are described by the kinetic model proposed by Albrand et al.²⁴ for sunflower oil hydrogenation (model introduced later). It was optimized from experiments performed in a stirred slurry reactor using the same

Pd/Al₂O₃ catalyst but in powder form. The authors noticed that the reaction was limited by internal pore diffusion (hence, an apparent kinetics was measured). However, a similar characteristic diffusion length for both the catalysts (powder and washcoat) allows the same rate laws to be applied in the present work. They are thus used as boundary conditions at the wall.

Simulation of Monotubes in Series. The simulation procedure then involves the following steps. The gas–liquid saturation section (after H₂ introduction) is first simulated where no reaction is considered at the wall, and the size of the unit cell remains unchanged (less than 5% of the initial quantity of H₂ being actually transferred in this section). Here, a sequential calculation is carried out. A steady state calculation of hydrodynamics is performed, and the obtained velocity field is then used for a transient simulation of H₂ mass transfer. This latter study is stopped when the UC has traveled 20 cm, which corresponds to the length of this monotube section. Indeed, the UC travels at U_{TP} which allows the determination of its position at any moment by time integration of the two phase velocity.

The catalytic section is then simulated, where hydrodynamics, mass transfer of all species, reactions at the wall, and bubble shrinkage are here all solved together by a transient simulation. The concentration fields of fatty acids are initially homogeneous and are deduced from their respective molar fraction in the sunflower oil before hydrogenation (Table S1). The initial concentration field of hydrogen is obtained from the previous study on gas–liquid saturation section.

Bubble shrinkage is calculated from the overall molar flux at the gas–liquid interface, Φ_{B,H_2} (eq 7). It comes with a reduction of the UC length that ensures the liquid volume surrounding the bubble remains constant. This implies that the length ratio of lubrication film to liquid slug reduces as the bubble shrinks.

$$\Phi_{B,H_2} = \iint_{S_B} -D_{H_2-oil} \left(\frac{\partial c_{H_2}}{\partial z} \cdot n_z + \frac{\partial c_{H_2}}{\partial r} \cdot n_r \right) dS_B \quad (7)$$

Additionally, gas retention, ϵ_G , is deduced at any moment from time integration of Φ_{B,H_2} which allows us to update the bubble and UC velocities (U_B and U_{TP} , respectively) during the simulation (eqs 3–5).

Simulations are carried out over the total channel length of the catalytic section (40 cm) and beyond. Nevertheless, meshing quality eventually decreases due to the UC size reduction. A criterion is set on mesh distortion to stop the calculation when mesh reaches a critical deformation which could affect its quality (Supporting Information for more details).

Prediction of Physical Properties. Density and surface tension of sunflower oil, ρ_L and σ_L , respectively, are linear functions of temperature.³⁷ On the other hand, density does not vary significantly with the saturation degree of the oil,³⁸ while no information could be found on the surface tension of partially hydrogenated oils. Thus, both were considered unchanged during the hydrogenation.

Density measurements of refined sunflower oil were performed between 20 and 100 °C using an Anton Paar 4100 M density meter. Linear regression of the data points yielded eq 8, where ρ_L is in kg m⁻³. The surface tension of the oil was measured with a Krüss DSA100 tensiometer between 20 and 78 °C, resulting in eq 9 where σ_L is in N m⁻¹. In both equations, T is the temperature expressed in degrees Celsius, and these expressions were extrapolated beyond their strict temperature range of application when needed.

$$\rho_L = 933 - 0.667T \quad (8)$$

$$\sigma_L = 0.0357 - 1.01 \times 10^{-4}T \quad (9)$$

In order to consider the strong coupling between transfer phenomena, the viscosity dependency to the saturation degree of the oil is introduced in eq 10 for μ_L . In this expression, X is defined by eq 2 and is calculated locally from the concentration field, while K'_0 , K'_1 , and K'_2 depend on temperature only.²³

$$\ln \mu_L = K'_0 + K'_1 X + K'_2 X^2 \quad (10)$$

Diffusivities of H₂ and TAG in the partially hydrogenated oil are also computed locally, using eqs 11 and 12, respectively, for a given temperature and viscosity.²³ Diffusivity coefficients are in m² s⁻¹, T in K, and μ_L in Pa s. In eq 11 M_{oil} is the molar mass of the oil in g mol⁻¹, and V_{H_2} is the molar volume of hydrogen at its bubbling point (equal to 0.0143 m³ kmol⁻¹). Parameters Θ and n_1 are equal to 42 and 0.6, respectively.²³ In eq 12, A and n_2 are equal to 7.72×10^{-16} (SI) and 1.2, respectively.²³

$$D_{H_2-oil} = \frac{1.858 \times 10^{-15} (\Theta M_{oil})^{0.5} T}{\mu_L^{n_1} V_{H_2}^{0.6}} \quad (11)$$

$$D_{TAG-oil} = \frac{AT}{\mu_L^{n_2}} \quad (12)$$

Reaction Scheme. A plausible mechanism for sunflower hydrogenation was investigated by Albrand et al.²⁴ that can be summed up in Figure 5, where L , C , T , and S stand for C18:2, *cis* C18:1, *trans* C18:1, and C18:0 fatty acids, respectively.

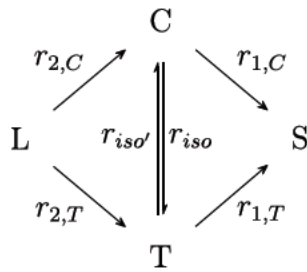


Figure 5. Simplified reaction scheme.

The production/consumption rates of each species are deduced from the previous reaction scheme and are given by eqs 13–17 (where r is expressed in mol s⁻¹ kg_{p,d}⁻¹).

$$r_L = -(r_{2,C} + r_{2,T}) \quad (13)$$

$$r_C = r_{2,C} - r_{iso} + r_{iso'} - r_{1,C} \quad (14)$$

$$r_T = r_{2,T} + r_{iso} - r_{iso'} - r_{1,T} \quad (15)$$

$$r_S = r_{1,C} + r_{1,T} \quad (16)$$

$$r_{H_2} = -(r_{2,C} + r_{2,T} + r_{1,C} + r_{1,T}) \quad (17)$$

This model is based on the Horiuti–Polanyi mechanism, which translates into a distinct dependency of saturation reactions ($r_{2,C}$, $r_{2,T}$, $r_{1,C}$ and $r_{1,T}$) and isomerization reactions (r_{iso} and $r_{iso'}$) on the hydrogen concentration over the catalyst surface, in accordance with experimental observations.⁷ Saturation reactions are proportional to θ_H (catalyst coverage fraction of H₂) as shown by eqs 18–21, and isomerization reactions are proportional to $(1 - \theta_H)$ (eqs 22 and 23).

$$r_{2,C} = \alpha \frac{\phi}{1 + \phi} \kappa_2 \theta_L \theta_H \quad (18)$$

$$r_{2,T} = \alpha \frac{1}{1 + \phi} \kappa_2 \theta_L \theta_H \quad (19)$$

$$r_{1,C} = \alpha \kappa_1 \theta_C \theta_H \quad (20)$$

$$r_{1,T} = \alpha \kappa_1 \theta_T \theta_H \quad (21)$$

$$r_{iso} = \alpha \kappa_{iso} \theta_C (1 - \theta_H) \quad (22)$$

$$r_{iso'} = \alpha \frac{\kappa_{iso}}{K_{iso}} \theta_T (1 - \theta_H) \quad (23)$$

Here, θ_H is considered for a dissociative adsorption of H₂. The expressions of the coverage fractions (θ_H , θ_L , θ_C , θ_T) and kinetic constants (κ_2 , κ_1 , and κ_{iso}), together with the thermodynamics constants (ϕ and K_{iso}), are available in Albrand et al.²⁴

To describe the catalyst deactivation experimentally observed in the single channel reactor (see experimental section), a coefficient α is introduced to weight the reaction rates (eqs 18 and 23). Values of α below 1 thus stand for a reduced catalyst activity.

Solved Equations. As stated above, only the liquid phase is simulated. Hence, velocity field in laminar flow ($Re < 840$) is obtained by solving the Navier–Stokes equations for an incompressible fluid (eqs 24 and 25).

Continuity equation:

$$\nabla \cdot (\rho_L \mathbf{u}) = 0 \quad (24)$$

Momentum equation:

$$\frac{\partial \rho_L \mathbf{u}}{\partial t} + \rho_L (\mathbf{u} \cdot \nabla) \mathbf{u} = -\nabla P + \nabla \cdot [\mu_L (\nabla \mathbf{u} + \nabla \mathbf{u}^T)] + \rho_L \mathbf{g} \quad (25)$$

Here, oil density remains constant, while its viscosity is evaluated locally through eq 10 for a given local saturation degree.

Mass transport of H₂ and fatty acids within the liquid is described by the convection–diffusion equation available in eq 26.

$$\frac{\partial c_i}{\partial t} + \nabla \cdot (-D_{i-oil} \nabla c_i) + \mathbf{u} \cdot \nabla c_i = 0 \quad (26)$$

Similarly, diffusivity is calculated locally for hydrogen and TAG according to eqs 11 and 12 for a given viscosity.

The moving mesh approach adopted in this work uses the arbitrary Lagrangian–Eulerian (ALE) method directly available in COMSOL MULTIPHYSICS. This method was originally developed by Noh³⁹ and Hirt et al.⁴⁰ and later applied to finite

elements in the context of viscous and incompressible flows.⁴¹ The ALE method allows one to keep an Eulerian description of the quantities of interest (fluid velocity, pressure, concentrations), while enabling deformation of the calculated domain within a fixed frame of reference (Lagrangian formulation).

From a practical standpoint, specific velocities are applied at the boundaries, inducing mesh displacement inside the considered domain. As a consequence, this moving mesh approach has the advantage to track precisely the domain boundaries, which is crucial near the gas–liquid interface. However, substantial domain deformation may result in the presence of inverted cells which will eventually stop the calculation.

In this work, contraction velocities of lubrication film and UC lengths have to be known. They are deduced from the bubble volume shrinkage velocity given by eq 27, where hydrogen is considered as a perfect gas.

$$\frac{dV_B}{dt} = \Phi_{B,H_2} \frac{RT}{P_{H_2}} \quad (27)$$

Since the total liquid volume in the UC does not vary, the UC volume variation equals that of the bubble. Hence, UC length contraction velocity is given by eq 28. Considering that the bubble has an ideal shape, its volume can easily be expressed as a function of L_f yielding the contraction velocity of the lubrication film (see eq 29, where $R_B = R_C - \delta_f$).

$$\frac{dL_{UC}}{dt} = \frac{1}{\pi R_C^2} \frac{dV_B}{dt} \quad (28)$$

$$\frac{dL_f}{dt} = \frac{1}{\pi R_B^2} \frac{dV_B}{dt} \quad (29)$$

Boundary Conditions. Mass Transport. For H_2 , saturation concentration $c_{H_2}^*$ (at thermodynamic equilibrium) is set at the gas–liquid interface according to eq 30, where H_0 and ΔE are equal to $1.13 \times 10^{-4} \text{ mol m}^{-3} \text{ Pa}^{-1}$ and 5 kJ mol^{-1} , respectively.⁴²

$$c_{H_2}^* = H_0 \exp\left(\frac{-\Delta E}{RT}\right) P_{H_2} \quad (30)$$

Preliminary studies showed that this Dirichlet condition can induce inaccuracy in flux evaluation with mesh displacement near the caps. To overcome this problem, weak constraints were activated for a more accurate estimation; they rely on Lagrangian multiplier to calculate the flux instead of an approximation of the spatial derivative based on the mesh.

A zero flux was imposed at the interface for fatty acids, due to their negligible volatility.

Periodic conditions were established for all species at the top and bottom of the UC. Concentration profiles were then identical at both boundaries.

As mentioned earlier, the catalytic washcoat is implemented by a simple boundary on which local flux densities for all species, $\phi_{W,i}$ are directly obtained from the apparent reaction rates (eqs 13–17), calculated with local concentrations at the wall, and washcoat characteristics (eq 31). Washcoat thickness (δ_C), apparent washcoat density (ρ_S), and metal content (w_{Pd}) values were discussed in the experimental section and are equal to $10 \mu\text{m}$, 750 kg m^{-3} , and $0.7 \text{ wt } \%$, respectively.

$$\phi_{W,i} = r_i \delta_C \rho_S w_{Pd} \quad (31)$$

Moving Mesh. The computed domain representing the liquid phase in the unit cell is divided in subdomains as shown in Figure 6. This partition allows one to precisely target where deformations occur.

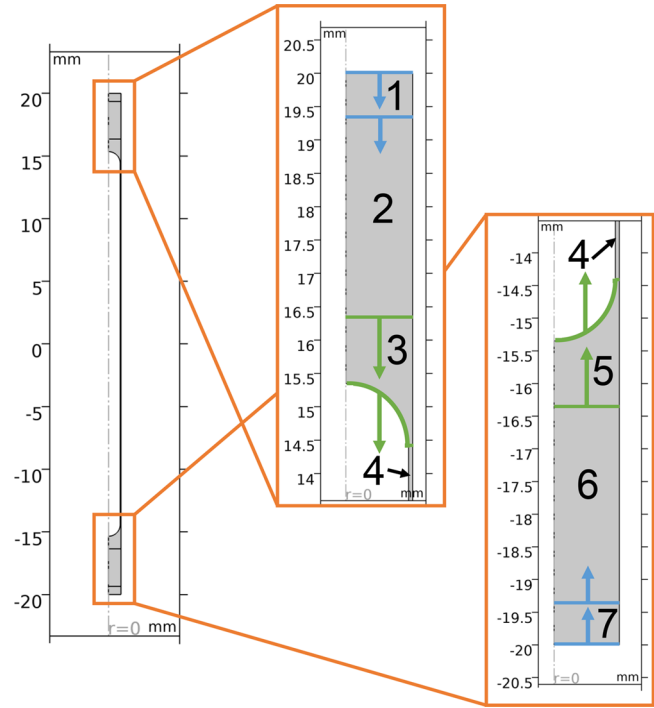


Figure 6. Division of the unit cell in subdomains. Boundaries motions set in the moving mesh physics are illustrated by the green arrows for the caps and the blue arrows for the UC ends.

Zero normal displacement is set for vertical boundaries (wall, lubrication film, and axial symmetry axis).

Horizontal boundaries for subdomain #1 at the top of the UC are set to move at $-1/2 dL_{UC}/dt$. Conversely, horizontal boundaries for subdomain #7 move at $+1/2 dL_{UC}/dt$.

In a similar way, curved and horizontal boundaries for the cap subdomains #3 and #5 displace at $-1/2 dL_f/dt$ and $+1/2 dL_f/dt$, respectively.

It means that subdomains #1, #3, #5, and #7 are to slide along the symmetry axis without any mesh deformation. However, the lubrication film subdomain (#4) is compressed axially over time, while subdomains #2 and #6 are stretched axially in order to maintain the overall liquid volume inside the unit cell. Figure 6 shows the displacement imposed to the moving boundaries.

Hydrodynamics. The slip boundary condition is set at the gas–liquid interface. At the wall, a no slip boundary condition with a wall moving at U_B (with $U_B > 0$) is implemented since the overall direction of the flow is descending. It is recalled that U_B is updated during calculation since ϵ_G is determined at any time through time integration of Φ_{B,H_2} .

Periodic conditions between top and bottom boundaries of the UC are usually adopted. Nevertheless, when these boundaries are moving, simply equaling the velocity profiles led to inconsistencies related to mass conservation of the TAG within the UC despite calculation convergence being reached. Therefore, the by default periodic condition of COMSOL was not applied for hydrodynamics, and appropriate boundary conditions were set manually (more details on the modified

boundary conditions are available in the [Supporting Information](#)).

Meshing and Numerical Parameters. Subdomains #2, #4, and #6 ([Figure 6](#)) subjected to deformations were meshed using quadrilateral elements since this mesh geometry withstands better axial compression or stretching than triangular elements. Such triangles were used for subdomains #3 and #5 to mesh the curved boundaries of the caps.

On the other hand, free meshes (triangles) were chosen for top and bottom subdomains (#1 and #7), since the general extrusion operator used to set the hydrodynamics boundary conditions works with such mesh type.

In addition, boundary layer meshing was set at the gas–liquid interface and at the wall, where sharp mass gradients are expected. Such a mesh type consists of rectangles aligned with the boundary allowing orthogonal meshing refinement. In order to apply a convenient grid resolution to describe the concentration gradients, a mesh sensitivity study was carried out; details are available in the [Supporting Information](#).

Finally, Lagrange polynomials of different orders were used for variable interpolation depending on the physics: linear and quadratic discretizations were selected for pressure and velocity, respectively, while cubic polynomials were used for concentrations. Additionally, a second order Laplace smoothing method was used for the calculation of mesh displacement.

Postprocessing Calculations. Overall molar fluxes of H_2 and fatty acids at the wall are calculated by [eqs 32](#) and [33](#).

$$\Phi_{W,H_2} = \iint_{S_W} -D_{H_2-oil} \left(\frac{\partial c_{H_2}}{\partial z} \cdot n_z + \frac{\partial c_{H_2}}{\partial r} \cdot n_r \right) dS_W \quad (32)$$

$$\Phi_{W,FA_i} = \iint_{S_W} -D_{TAG-oil} \left(\frac{\partial c_{FA_i}}{\partial z} \cdot n_z + \frac{\partial c_{FA_i}}{\partial r} \cdot n_r \right) dS_W \quad (33)$$

Average concentrations in the UC liquid and on the catalytic wall for any species i are given by [eqs 34](#) and [35](#), respectively.

$$c_{L,i} = \frac{\iiint_{V_L} c_i dV_L}{\iiint_{V_L} dV_L} \quad (34)$$

$$c_{W,i} = \frac{\iint_{S_W} c_i dS_W}{\iint_{S_W} dS_W} \quad (35)$$

Cases Studied. All cases presented in [Table 2](#) were simulated using COMSOL MULTIPHYSICS version 5.6. The results were obtained with a PC running 64 bit Windows 10 (Intel Xeon CPU W 2123 @ 3.60 GHz, 128 Gb RAM). As discussed earlier, an initial UC length ($L_{UC,0}$) of 40 mm was chosen by default, but another length of 20 mm was also tested for Case 1 (see [Case 1b](#)).

Finally, since severe catalyst deactivation was observed during the experimental hydrogenation campaign, simulations were carried out for different catalyst activity levels (α ranging from 1 to 0.1). An overall number of nine calculations was achieved.

RESULTS AND DISCUSSIONS

Numerical Results. Preliminary Gas–Liquid Saturation. Results for the monotube section where only mass transfer of H_2 occurs (without bubble shrinking) are discussed here.

Hydrogen concentration fields and streamlines near the bubble nose and tail obtained at this section outlet are displayed

in [Figure 7](#) for Case 1a. It exhibits the characteristic Taylor flow vortices in the liquid slugs and lubrication film between the bubble and the wall.⁴³

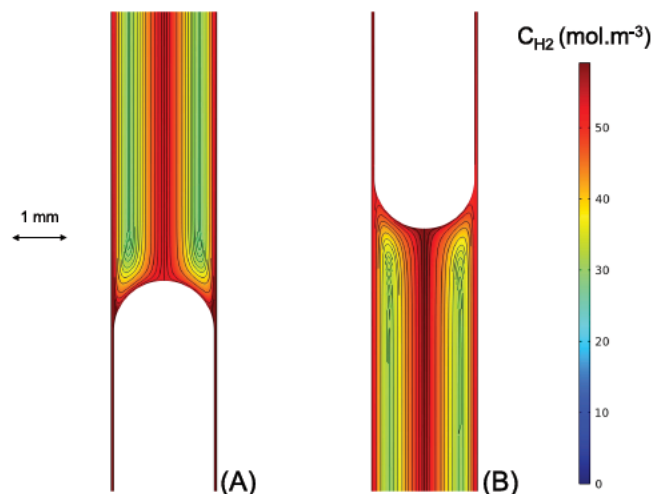


Figure 7. Hydrogen concentration field and streamlines around the bubble caps at the outlet of the gas–liquid saturation section for Case 1a: bubble tail (A) and bubble nose (B).

As described by Thulasidas et al.,⁴⁴ stagnation points are observed at the edge of both caps. The outermost vortex streamline which connects these stagnation points and separates recirculating flow from the liquid film in the slug is called the dividing streamline ([Figure S2, Supporting Information](#)). Since the overall direction of the flow is descending, the vortex is recirculating in a counterclockwise direction; the liquid near the channel center is flattened against the rear cap tip, then goes along the liquid film until it reaches the edge of the nose cap and finally moves back to the channel center by lapping the cap.

The liquid film (along the bubble body and in the liquid slugs) is highly saturated. Likewise, the fluid on the dividing streamline is also saturated, as shown by the solute concentration at the channel center, near the caps, and in the liquid film. Conversely, H_2 concentration at the vortex center is the lowest in all the liquid.

However, the description proposed by Yang et al.,⁴⁵ where gas–liquid mass transfer in Taylor flow is first driven by the convective effect of the vortex and then by the diffusion perpendicular to the streamlines to saturate the vortex center, must actually be qualified to some extent. Indeed, the concentration difference observed at the channel center between the nose and the tail of the bubble indicates that the radial diffusion of the solute is already significant. Hence, convection and diffusion phenomena occur simultaneously.

It is worth noting that 74% of H_2 saturation is reached in the liquid at the outlet of this uncoated section for Case 1a. Twice shorter $L_{UC,0}$ yields 81% ([Case 1b](#)). Similarly, in all investigated cases, the relative saturation ranges from 71 to 81%.

Catalytic Section. Numerical Results. To simulate this section, catalytic reactions at the wall and moving mesh for bubble shrinking are activated. It is recalled that the H_2 concentration field is initialized with the previous section results, while the “initial” concentrations of fatty acids are supposed to be homogeneous and equal to those in the edible oil feed ([Table S1](#)). Although the catalytic reactor is 400 mm long,

the simulations are carried out beyond this length to evaluate the reaction selectivity over a higher saturation degree.

To save computational time, only PUFA and *cis* and *trans* MUFA concentration fields are solved; SFA is then deduced from local mass balance.

H₂ and PUFA concentration fields at different positions of the UC are given in Figure 8.

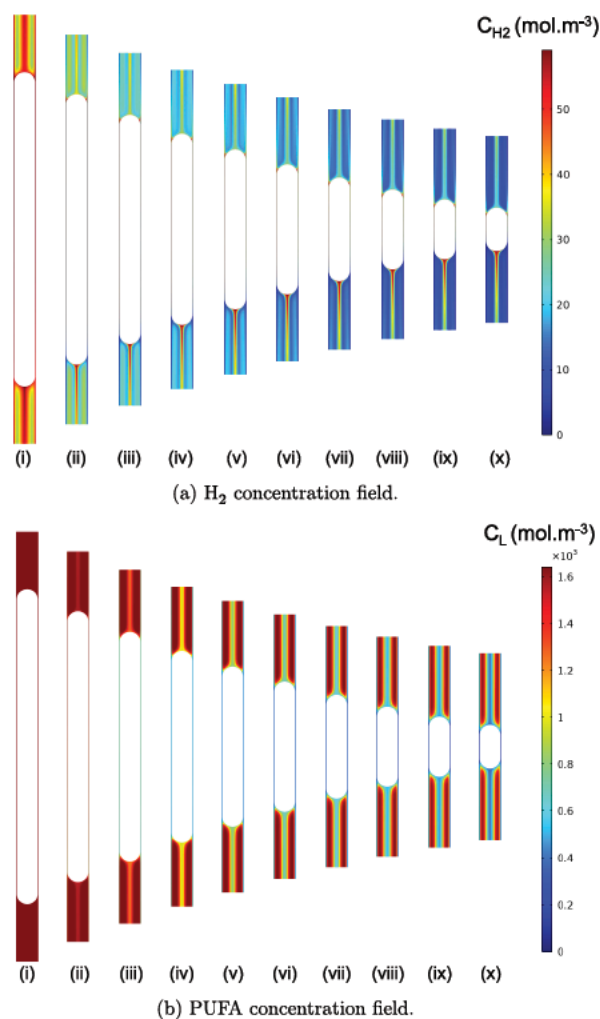


Figure 8. H₂ (a) and PUFA (b) concentration fields with shrinking bubble/UC for Case 1a, $\alpha = 1$ at different UC positions: (i) $z = 0$ mm, (ii) $z = 100$ mm, (iii) $z = 200$ mm, (iv) $z = 300$ mm, (v) $z = 400$ mm, (vi) $z = 500$ mm, (vii) $z = 600$ mm, (viii) $z = 700$ mm, (ix) $z = 800$ mm, and (x) $z = 900$ mm.

It first illustrates the significant bubble shrinkage observed over the catalytic section of the experimental setup (here, $z = 400$ mm), ϵ_G varying from 0.64 to 0.47. Moreover, concentration gradients of H₂ and especially of PUFA become more prominent as the reaction progresses.

Figure 9a shows the evolution of the UC length as a function of its position from the entrance of the catalytic section. As expected, the higher the catalytic activity the faster the decrease of L_{UC} for given operating conditions. This diminution is also faster near the reactor inlet. This indicates that the gas–liquid flux at the bubble interface slows down along the channel.

On the other hand, when plotting L_{UC} with respect to the overall conversion X (Figure 9b), a linear decreasing trend is

observed, and the effect of catalyst activity, as well as that of temperature, are canceled. All that remains is P_{H_2} effect, where the reduction of L_{UC} is twice as fast at 10 bar (Case 4) versus 21 bar (other cases).

Figure 10 shows the evolution of the saturation degree of the oil with respect to the UC position. A comparison is made between the present simulations (Figure 10a) and those obtained where moving mesh is deactivated; hence, bubble and UC lengths are constant (Figure 10b). It is noted that any given X is reached for a shorter distance in the case of no bubble shrinkage. This can be explained by the fact that H₂ transfer at the gas–liquid interface is overestimated in this latter case since the bubble surface area remains constant. Consequently, superficial gas velocity, hence, U_{TP} , diminishes faster for constant bubble size, resulting in a higher residence time of the UC at a given position.

For instance, at $z = 400$ mm for the Case 1a with $\alpha = 1$, the saturation degree of the oil would reach 19.1% with a constant bubble size, while this value drops to 13.3% when accounting for the bubble shrinkage (hence, a 44% relative difference).

Concentration fields for H₂ and PUFA near the caps at $z = 400$ mm are available in Figure 11. As expected, both species are depleted near the wall: in the lubrication film and in the liquid slug.

Due to the direction of the recirculating flow discussed earlier (the bubble moving downward), high H₂ concentration is noted at the channel center close to the bubble nose, while for the rear cap the highest concentrations are located at the stagnation points.

These distinct upstream vs downstream concentration fields demonstrate the effect of the radial diffusion of the solute with a decreasing concentration along the channel center from the nose to the tail, as seen in the preliminary gas–liquid saturation section. In other words, the assumed hypothesis that concentration is homogeneous on a given vortex streamline⁴⁶ might be too simplistic for H₂, despite the Péclet number calculated by eq 36⁴⁷ being equal to 485, thus much higher than 1.

$$Pe_i = \frac{(U_{TP} - 1/2U_B)d_C^2}{L_S D_{i-oil}} \quad (36)$$

Conversely, the PUFA concentration field exhibits no such reduction of concentration along the channel axis. Thus, liquid species exhibit a uniform concentration on a given vortex streamline. This is explained by the much lower TAG diffusivity compared to H₂ ($D_{TAG-oil,0} = 3.9 \times 10^{-10}$ vs $D_{H_2-oil,0} = 2.1 \times 10^{-8}$ m² s⁻¹).

Furthermore, PUFA concentration field in the liquid exhibits the following characteristics:

- The concentration of C18:2 fatty acid is the lowest at the catalytic wall where they are consumed.
- The PUFA concentration inside the vortex center remains sensibly equal to their initial concentration.
- The channel center is sensibly less concentrated due to the recirculating streamlines which connect the catalytic wall and the channel center by passing along the bubble caps.

A closer inspection of the PUFA concentration field near the wall highlights steep radial mass gradients (Figure S1a). This trend matches the description of PUFA radial concentration profiles in half slugs made in Albrand et al.²³

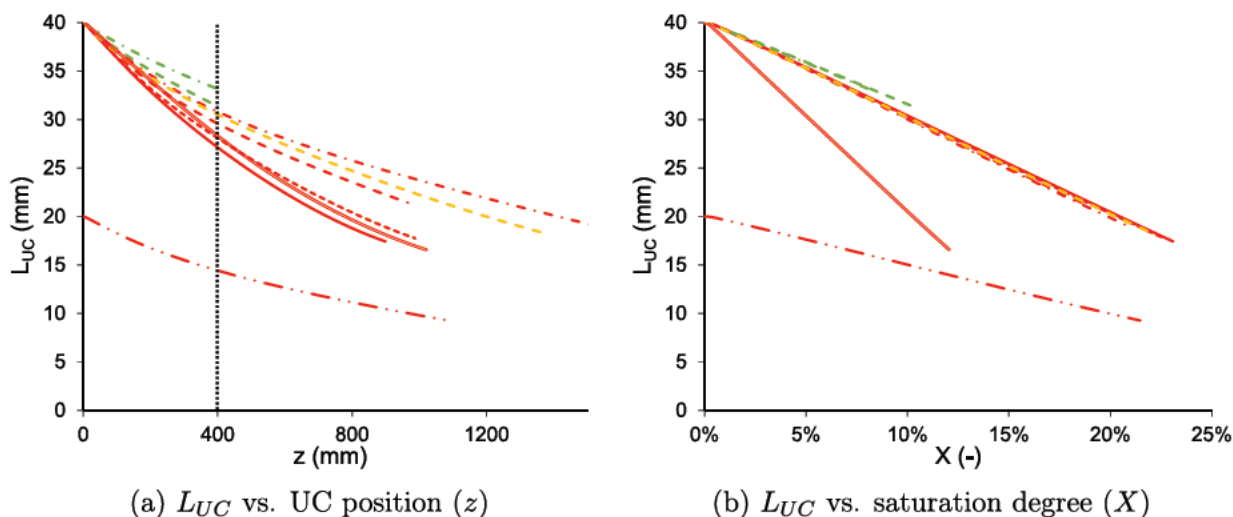


Figure 9. Calculated L_{UC} vs UC position (a) or saturation degree (b): 80 °C (green), 120 °C (orange), 160 °C (red); $\alpha = 1$ (—), 0.5 (---), 0.2 (- · -), 0.1 (· · ·); Case 1b (160 °C, 21 bar, $\alpha = 0.2$, $L_{UC0} = 20$ mm) (· · ·); Case 4 (160 °C, 10 bar, $\alpha = 0.1$) (=); length of the catalytic channel section $z = 400$ mm (vertical dotted line).

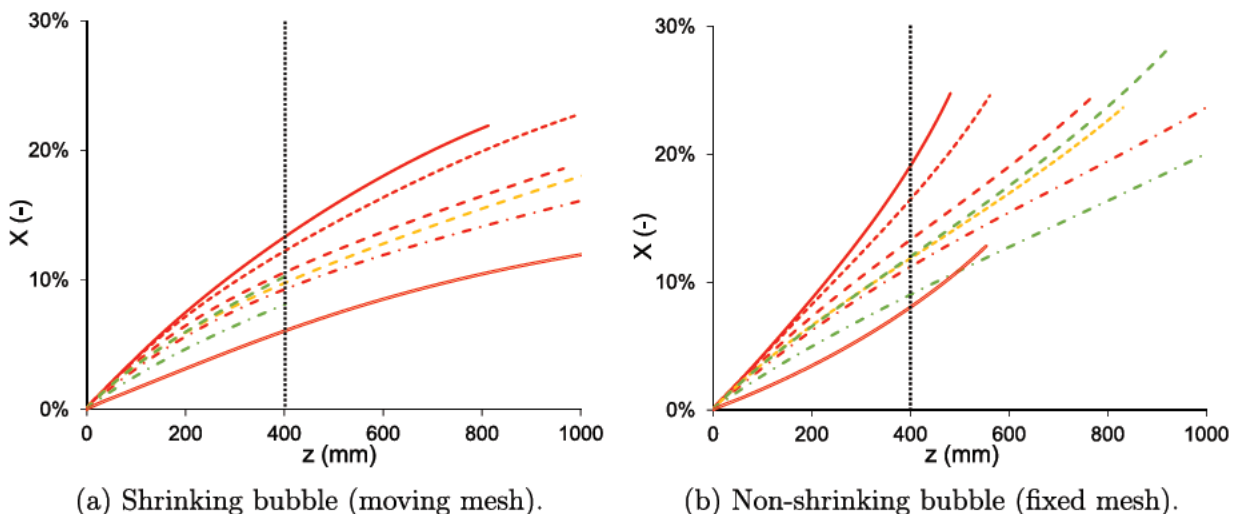


Figure 10. Calculated saturation degree of the oil (X) as a function of UC position (z) for a shrinking (a) and non-shrinking (b) bubble: 80 °C (green), 120 °C (orange), 160 °C (red); $\alpha = 1$ (—), 0.5 (---), 0.2 (- · -), 0.1 (· · ·); Case 4 (160 °C, 10 bar, $\alpha = 0.1$) (=); length of the catalytic channel section $z = 400$ mm (vertical dotted line).

As a consequence, notable differences are present between the average concentrations in the liquid and the average concentrations at the wall for Case 1a, $\alpha = 1$ (Figure 12a and b). At the wall, a very sharp decrease of H_2 concentration is noted at the reactor inlet. The gaseous solute is here the limiting species, which induces the isomerization of the *cis* MUFA into *trans* MUFA. Maximal overall MUFA concentration is reached at $z = 125$ mm. At this point, PUFA start to be the limiting species, and H_2 concentration at the wall increases. Here, *cis* and *trans* MUFA are consumed in turn, yielding a rise in SFA concentration at the wall. This fast limitation of the liquid species at the wall has been previously described in Albrand et al.²³ It is exacerbated by the decrease in their diffusivity as the reaction progresses. This PUFA depletion at the wall results in virtually no increase in the *cis* MUFA fraction in the liquid, while SFA production is high.

For $z > 400$ mm, H_2 concentration at the wall drops again to the point that it once again becomes the limiting species, as demonstrated by the concentration rise of all unsaturated fatty

acid for $z = 650$ mm. This behavior was not noticed in Albrand et al.²³ It can be explained by the fact that the bubble shrinkage is accounted for here; the bubble length, and thus the available surface area for gas–liquid mass transfer, finally reach a critical value where the overall solute mass transfer can no longer supply for the reaction need.

Figure 12c and d show also the average concentrations in the liquid and at the wall for the same operating conditions but with a reduced catalyst activity (Case 1a, $\alpha = 0.1$). Unlike the $\alpha = 1$ study case, H_2 never becomes the limiting species. Thus, there is no reduction in *cis* MUFA concentration at the very inlet of reactor as previously observed, and their concentrations remain above that of *trans* MUFA until PUFA are depleted at the wall. At this point, *cis* MUFA production, which mainly comes from PUFA hydrogenation,²⁴ slows, and a *cis* to *trans* isomerization reaction takes over.

Nonetheless, the net production of *cis* MUFA remains almost imperceptible in the liquid bulk as found for $\alpha = 1$.

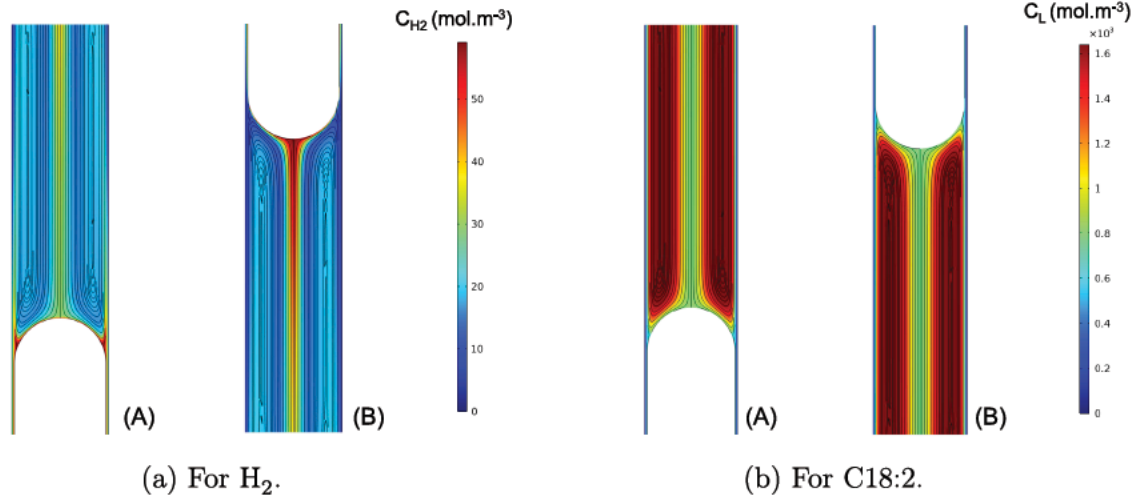


Figure 11. Hydrogen (a) and C18:2 (b) concentration fields and streamlines around the bubble caps at the catalytic section outlet ($z = 400$ mm) for Case 1a, $\alpha = 1$: bubble tail (A) and bubble nose (B).

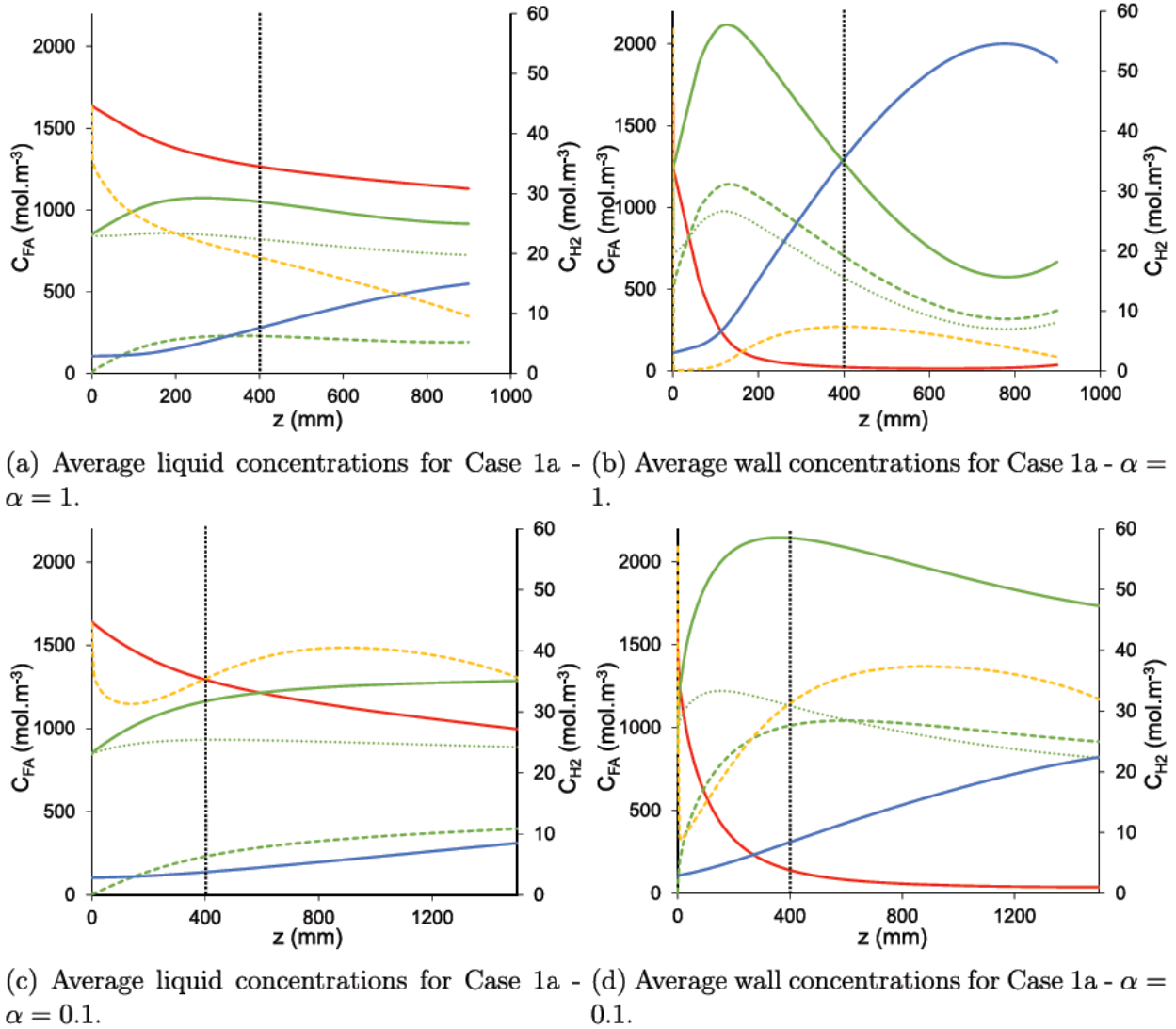


Figure 12. Average concentrations of fatty acids and H₂ in the liquid (a, c) and at the wall (b, d) for Case 1a (160 °C, 21 bar, $L_{UC0} = 40$ mm), $\alpha = 1$ (a, b) and $\alpha = 0.1$ (c, d): C18:2 (red —), overall C18:1 (green —), *cis* C18:1 (green ...), *trans* C18:1 (green - - -), C18:0 (blue —), H₂ (yellow - - -, second axis); length of the catalytic channel section $z = 400$ mm (vertical dotted line).

Table 3. Comparison between Simulated Compositions and Average Measured Values in Hydrogenated Oil at the Reactor Outlet

Assay	x_L (% mol)		x_C (% mol)		x_T (% mol)		x_S (% mol)		X (%)		
	Exp, ave	CFD ^a	Exp, ave	CFD ^a							
Activation											
MT1 C1 A1	42.9	45.1	33.0	29.3	7.4	8.1	8.9	9.9	14.0	13.3	
MT1 C1 A2	47.7	45.3	30.5	31.9	5.5	9.2	8.5	6.0	10.4	10.6	
MT1 C1 A3	53.1	46.1	30.1	33.2	2.2	8.2	7.0	4.9	5.6	9.3	
Cleaning and reactivation											
MT1 C2 A1	52.1	46.1	29.7	33.2	3.3	8.2	7.2	4.9	6.4	9.3	
Activation											
MT2 C3 A1	40.8	45.1	32.3	29.3	8.7	8.1	10.5	9.9	16.4	13.3	
MT2 C3 A2	47.8	47.0	30.2	31.8	4.1	7.1	10.2	6.5	11.4	9.7	
MT2 C3 A3	52.7	48.6	29.7	33.6	1.6	4.6	8.3	5.7	6.8	8.1	
MT2 C3 A4	49.6	45.3	29.0	31.9	2.6	9.2	11.2	6.0	10.8	10.6	
MT2 C3 A5	52.4	49.8	29.6	31.7	2.4	6.9	7.9	4.0	6.7	6.1	

^aThe selection of CFD results (i.e., the corresponding values of α between 0.1 and 1) is based on the evolution of the saturation degree of the oil with respect to the time on stream (Table S3).

Comparison between Experimental and Numerical Results. Table 3 gives the experimental and simulation results obtained at $z = 400$ mm, regarding the composition and saturation degree of the hydrogenated oil. The former correspond to the averaged values calculated from all the samples analyzed for a given assay. Here, the molar fractions x_L , x_C , x_T , and x_S refer to the molar fractions of C18:2, *cis* C18:1, *trans* C18:1, and C18:0 fatty acids, respectively. The simulation results shown here are those whose α value gives the best fit with the measured saturation degree. All the numerical results and the discussion on the effect of $L_{UC,0}$ (Case 1b vs Case 1a) are detailed in the Supporting Information (Table S3).

For the two pairs of monotubes, the highest saturation degrees were achieved during the first experiment at 160 °C and 21 bar (MT1–C1–A1 and MT2–C3–A1). They were close to 15% for both the pairs. Corresponding simulation (Case 1a) with $\alpha = 1$ predicts $X = 13.3\%$.

Significant catalyst deactivation occurred for the MT1 pair, as shown by the progressive reduction of X in the subsequent experiments carried out in the same operating conditions (cf. Figure 4 and Table 3). Its activity was, however, partially recovered after cleaning with decane and reduction under H_2 , as it can be seen for the MT1–C2–A1 assay. The calculated saturation degree of the oil drops as low as 9.3% in Case 1a when α was set to 0.1, which is higher than the lowest observed conversion measured in the pilot unit ($X = 5.6\%$). For other operating conditions, relative differences between experimental and numerical results range between 9% and 19%.

Looking at the composition in fatty acids, the *cis* MUFA fraction appears relatively well represented by the CFD model. However, PUFA and SFA fractions are usually underestimated, except for the highest activity of the catalyst at 160 °C and 21 bar (MT1–C1–A1 and MT2–C3–A1). Conversely, the TFA fraction is always overestimated by the model (except for assay MT2–C3–A1).

Finally, Figure 13 compares the molar fraction of fatty acids predicted by the simulation and measured in all the collected samples as a function of the saturation degree of the oil. PUFA, MUFA (with no *cis/trans* distinction), and SFA data are available in Figure 13a, b, and c, respectively. For these three fatty acids, all the simulations (eventually with different α values) exhibit the same behavior for $X < 5\%$: x_L and x_M evolve in

the same proportions but in an opposite way, while x_S stagnates. This behavior obeys the reaction kinetics where PUFA are hydrogenated first when highly concentrated.

For $X > 5\%$, the resistance to the external mass transfer of the TAG starts to affect the species production/consumption rates at the catalyst wall. When PUFA become the limiting species, MUFA are consumed in turn, which is enhanced by a high catalyst activity. Temperature impacts external resistance as well, but it is however difficult to compare the 160, 120, and 80 °C cases, since distinct flow rates were also set for these experiments.

Calculated MUFA fraction in Case 4 (160 °C, 10 bar) remains high for large X values. This can be explained by the fact that H_2 is always the limiting species in this case due to the moderate pressure. Thus, all saturation reactions are impacted identically. The effect of restrained H_2 supply is also visible—but to a lesser extent—for X above 20%, where x_M consumption is slightly slowed. This is due to late H_2 limitation occurring at the wall when the bubble length reaches a critical value, as discussed earlier.

Overall, the predicted fractions are in the same order of magnitude as the measured ones, albeit not perfectly fitting the observed trends. For instance, SFA production starts earlier in the hydrogenation experiments, and their molar fraction increases linearly with X , while simulations display a quick rise only after $X > 5\%$. This might question the assumed equivalence between the monotube washcoat and the catalyst powder used in Albrand et al.²⁴ to establish the kinetic model (with respect to the catalyst selectivity and/or internal diffusion resistance).

Concerning *cis/trans* distribution, simulations predict that *trans* MUFA increase at the expense of *cis* compounds, limiting the maximal molar fraction of the latter to 34% in the investigated conditions (Figure 13d). Thus the x_T to x_C ratio essentially follows the same trend as x_T for $X < 10\%$, since the x_C increase is very small (Figure 13f). If the calculated x_C values are similar to those reached experimentally, x_M and x_T are however clearly overestimated by the model over this X range (Figure 13b and e). Moreover, the lower the catalyst activity is, the higher is the predicted x_C as found for the overall MUFA fraction (x_M). This trend differs from the experiments where the highest selectivity toward the *cis* compound at 160 °C and 21 bar was measured in the first samples, thus when the catalyst was the

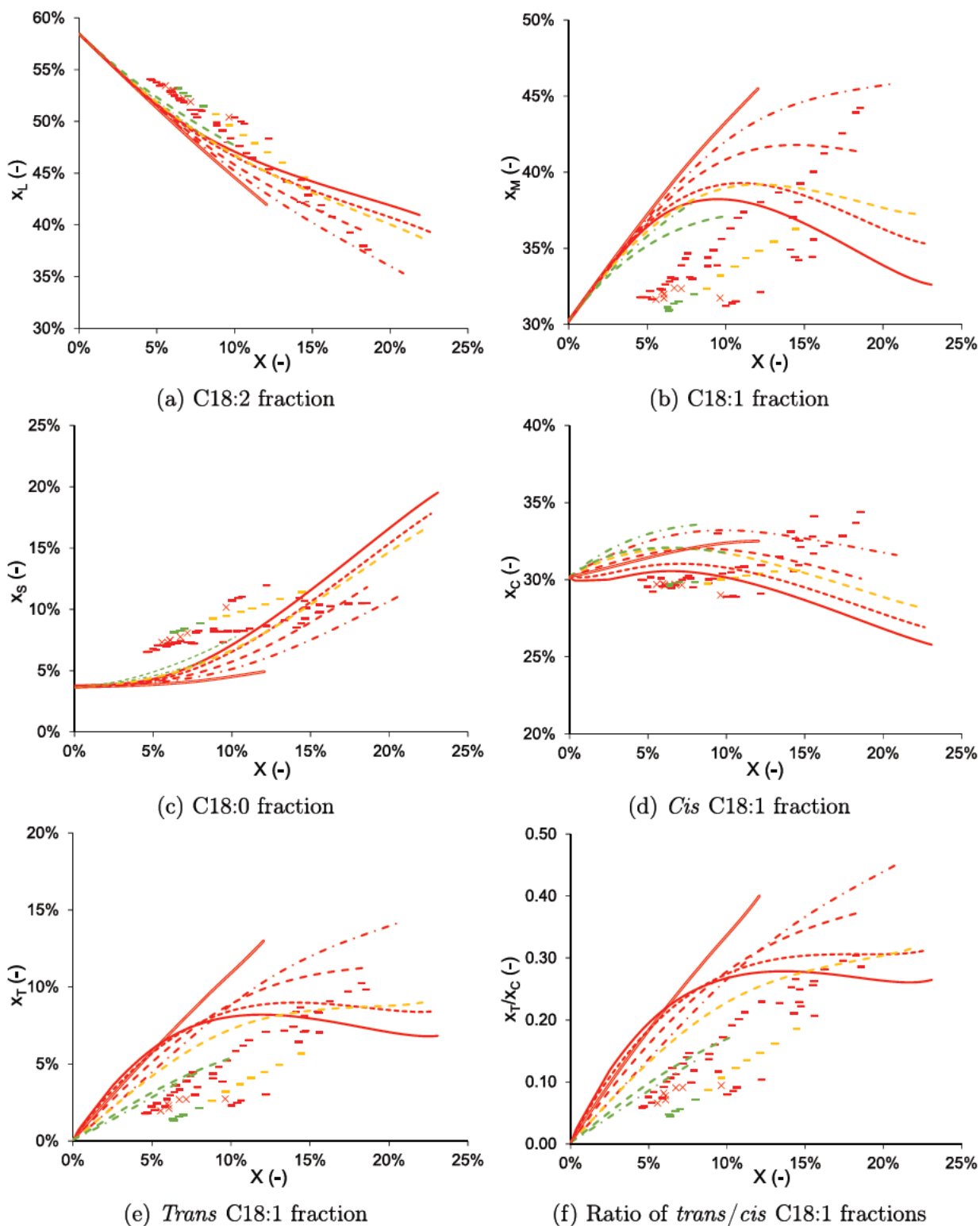


Figure 13. Comparison of single channel hydrogenation results (symbols) and CFD simulations (lines): molar fractions of the different fatty acids (a–e) and ratio of *trans* to *cis* MUFA fractions (f) vs the saturation degree of the oil (X): 80 °C (green), 120 °C (orange), 160 °C (red); 10 bar (x), 21 bar (-); $\alpha = 1$ (—), 0.5 (- -), 0.2 (· ·), 0.1 (·); Case 4 (160 °C, 10 bar, $\alpha = 0.1$) (=).

most active. This emphasizes the possibility that external mass transfer resistances are not solely responsible for the modest performances of the single channel reactor. Catalyst deactivation might have also impacted reaction selectivity.

Evaluation of Mass Transfer Coefficients. Mass transfer coefficients are particularly useful for evaluating the limiting

phenomena in complex multistep processes, as well as for reactor presizing using simplified plug flow like models. Hence, this section aims to calculate these coefficients based on the numerical simulations and to compare the values with available correlations. Volumetric coefficients were deduced from mass transfer fluxes and previously shown concentration fields.

Table 4. Correlations Applied for Evaluation of Mass Transfer Coefficients

Interface	Equation
Gas wall	$k_{GS} = \frac{D_{H_2-oil}}{\delta_f}$
Gas slug ^a	$k_{GL} = \frac{2\sqrt{2}}{\pi} \sqrt{\frac{D_{H_2-oil} U_B}{d_C}}$
Slug wall ^b (H ₂ and TAG)	$[k_{LS}]_i = \left[\frac{1}{20 \frac{D_i-oil}{d_C} \left 1 + 0.003 \left(\frac{L_{UC} - L_f}{d_C Re_{TP} Sc_i} \right)^{-0.71} \right } + \frac{\delta_f}{D_i-oil} \right]^{-1}$

^aFrom van Baten and Krishna.³⁵ ^bFrom Kreutzer et al.⁴⁹

In detail, mean concentrations of fatty acids in the liquid and at the wall were obtained by eqs 34 and 35. For H₂, distinct concentrations were calculated according to the considered zone (Figure 6): the liquid slugs (subdomains #1, #2, #3, #5, #6, and #7 altogether) or the film (subdomain #4).

Likewise, interface regions were subdivided for the evaluation of “local” hydrogen molar fluxes. Therefore, at the gas–liquid interface, fluxes issued from the caps and the film were integrated separately, referred to as Φ_{caps,H_2} and Φ_{film,H_2} respectively. Additionally, discrimination at the wall was made between molar fluxes in the liquid slug and in the film, $\Phi_{W,slug,H_2}$ and $\Phi_{W,film,H_2}$ respectively (Figure S2, Supporting Information).

Volumetric coefficients for mass transfer of H₂ from the bubble cap to the liquid slug (“gas–liquid”), $k_{GL}a_{GL}$ from the liquid slug to the catalytic wall (“liquid–solid”), $[k_{LS}a_{LS}]_{H_2}$ and through the lubrication film directly to the wall (“gas–solid”), $k_{GS}a_{GS}$, were calculated by eqs 37–39.

$$k_{GL}a_{GL} = \frac{\Phi_{caps,H_2}}{c_{H_2}^* - c_{L,slug,H_2}} \frac{1}{V_{UC}} \quad (37)$$

$$[k_{LS}a_{LS}]_{H_2} = \frac{\Phi_{W,slug,H_2}}{c_{L,slug,H_2} - c_{W,slug,H_2}} \frac{1}{V_{UC}} \quad (38)$$

$$k_{GS}a_{GS} = \frac{\Phi_{film,H_2}}{c_{H_2}^* - c_{W,film,H_2}} \frac{1}{V_{UC}} \quad (39)$$

An overall liquid–solid mass transfer coefficient for TAG, $[k_{LS}a_{LS}]_{TAG}$, was obtained from eq 40, based on PUFA.

$$[k_{LS}a_{LS}]_{TAG} = \frac{\Phi_{W,film,FA_i} + \Phi_{W,slug,FA_i}}{c_{L,FA_i} - c_{W,FA_i}} \frac{1}{V_{UC}} \quad (40)$$

The corresponding specific surface areas were calculated by eqs 41–44.¹³ It is recalled that V_{UC} , L_{UC} and L_f were evaluated for each UC position.

$$a_{GS} = \frac{4d_B L_f}{d_C^2 L_{UC}} \quad (41)$$

$$a_{GL} = \frac{4d_B^2}{d_C^2 L_{UC}} \quad (42)$$

$$[a_{LS}]_{H_2} = \frac{4}{d_C} \left(1 - \frac{L_f}{L_{UC}} \right) \quad (43)$$

$$[a_{LS}]_{TAG} = \frac{4}{d_C} \quad (44)$$

Correlations available in the literature for the different interphase mass transfer coefficients are given in Table 4. It is noted that the same correlation was applied to evaluate the mass transfer of both TAG and hydrogen from the liquid slug to the catalytic wall. Indeed, very few correlations were reported for the case of liquid phase species, and the correlation of Hatziantoniou and Andersson⁴⁸ was previously found to overpredict fatty acid fluxes with respect to the values found by the CFD simulations (Albrand et al.²³). As a consequence, Kreutzer et al.’s⁴⁹ correlation, which was originally established for the transfer of a gas solute, was also considered here for the TAG.

A comparison between mass transfer coefficients calculated via the numerical simulations and via the correlations is given in Figures 14 and 15 for H₂ and TAG, respectively.

The gas–liquid coefficient, k_{GL} , exhibits a similar decrease along the reactor for both evaluations (from CFD and correlation) (Figure 14a and b). It originates mainly from the fast reduction of bubble velocity along the channel. Nevertheless, the correlation of van Baten and Krishna³⁵ leads to a slight underestimation with respect to the present CFD derived values, from 5% to 30% depending on the considered case.

The assumption that mass transfer in the lubrication film is mainly diffusive seems sound when comparing the value of k_{GS} calculated numerically with that obtained from the classical stagnant film model (Figure 14c and d). However, some underestimation by the latter is once again noted (between 14% and 24% at the channel outlet).

However, a further investigation of mass flux in the lubrication film highlights a notable difference between the fluxes evaluated at the gas–liquid interface and at the wall; only from 40% to 70% of the H₂ molar flux transferred from the lateral surface of the bubble is actually consumed at the opposite wall. Note that conversely this fraction remains above 90% when the bubble surface area is kept constant (by deactivating the moving mesh feature). Hence, bubble shrinkage seems to increase the solute mass transport from the lubrication film to the liquid slugs. Nirmal et al.⁴⁶ considered this so called *cross talk* in their analytical model describing gas–liquid mass transfer in Taylor flow conditions with no reaction. They showed that excluding cross talk could lead to an overprediction of k_{GL} , then solute diffusivity. The impact on the latter could be as high as a factor 3.5 when a homogeneous concentration in the liquid slug was also hypothesized.

This exchange between the liquid slugs and the lubrication film might explain the difference between the values of k_{LS,H_2} obtained from the CFD simulations and the equation proposed by Kreutzer et al.⁴⁹ (Figure 14e and f). Indeed, the latter equation only considers mass transfer resistance in series from the liquid vortex to surrounding stagnant liquid film in the slug

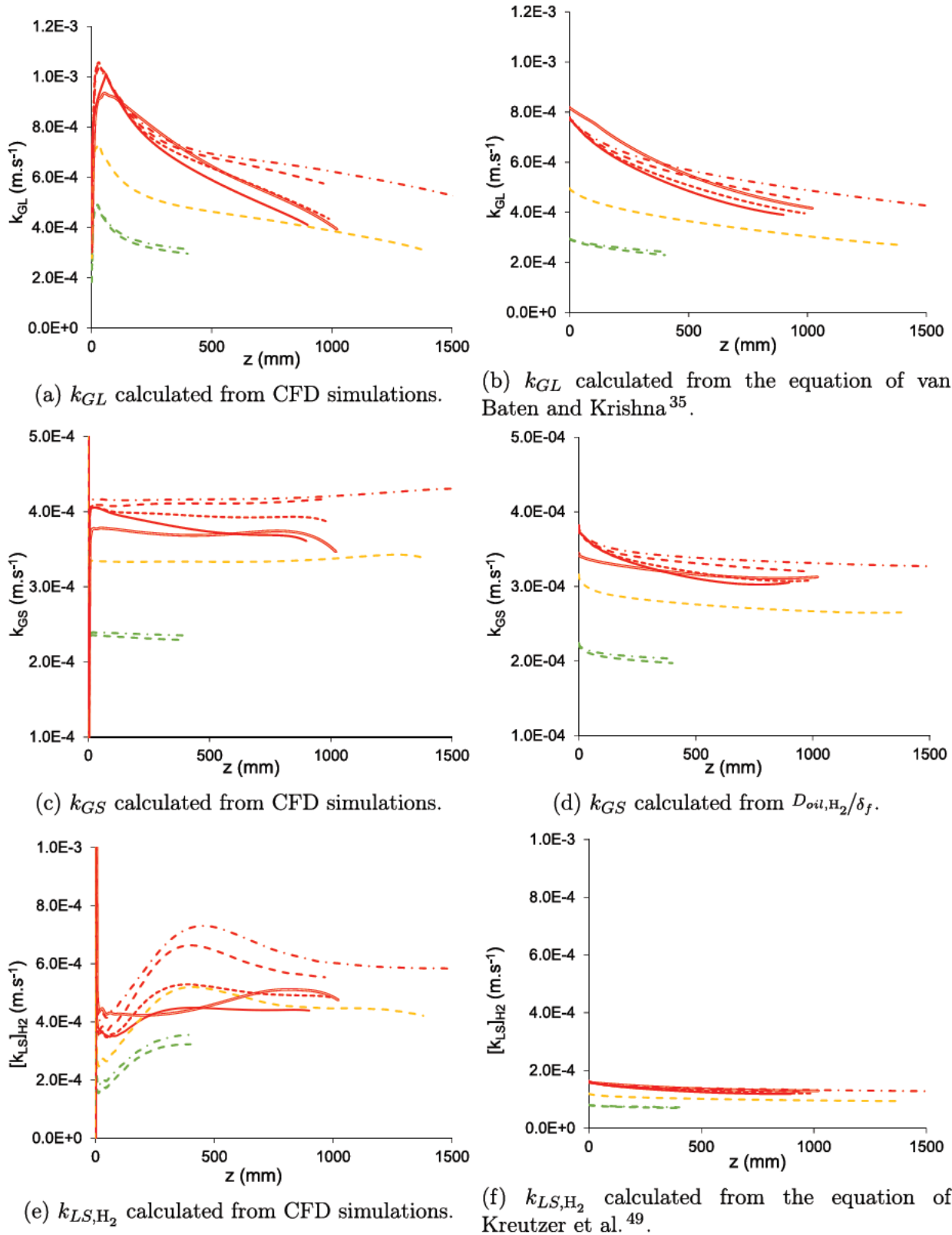


Figure 14. Mass transfer coefficients for H_2 — k_{GL} (a, b), k_{GS} (c, d), and k_{LS,H_2} (e, f), obtained from the simulations and from literature correlations: 80 °C (green), 120 °C (orange), 160 °C (red); $\alpha = 1$ (—), 0.5 (- -), 0.2 (- · -), 0.1 (· · ·); Case 4 (160 °C, 10 bar, $\alpha = 0.1$) (=).

and finally to the wall. As a consequence, k_{LS,H_2} is underestimated by up to a factor 5 by the correlation at the channel outlet.

Interestingly, the same equation gives satisfactory results for $k_{LS,TAG}$ after a given length (Figure 15a and b). Contrary to

hydrogen, fatty acids are quickly depleted near the wall and hence in the liquid film. Subsequently, cross talk contribution becomes rapidly negligible for the liquid phase species. The CFD derived values then reach those given by the correlation

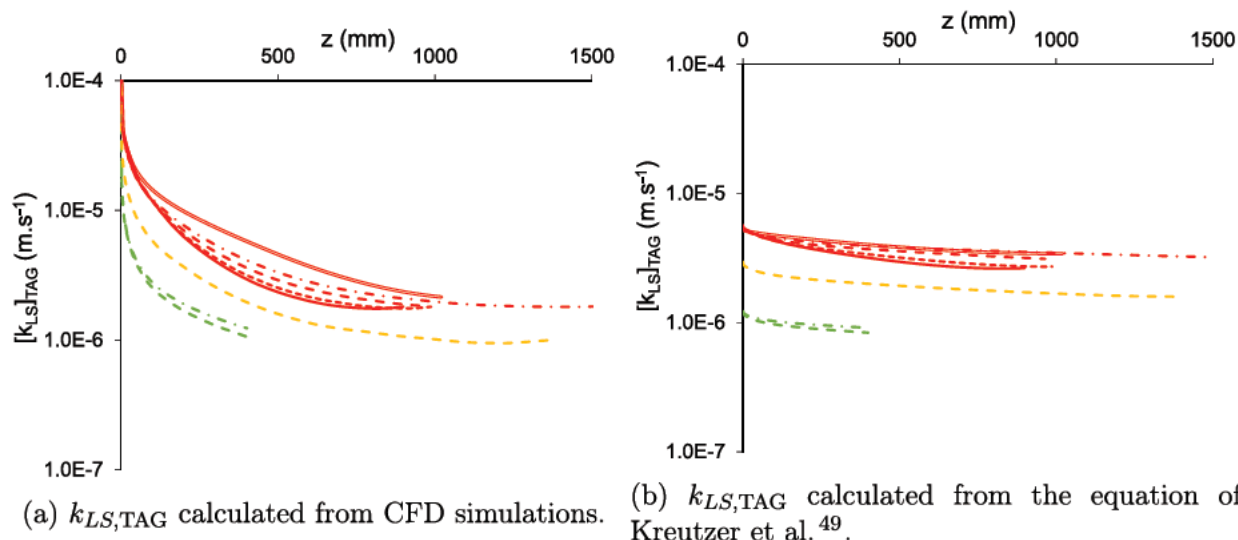


Figure 15. Mass transfer coefficients for TAG obtained from the simulations (a) and from literature correlation (b): 80 °C (green), 120 °C (orange), 160 °C (red); $\alpha = 1$ (—), 0.5 (---), 0.2 (···), 0.1 (— · —); Case 4 (160 °C, 10 bar, $\alpha = 0.1$) (=).

and even become lower at the channel outlet. A possible explanation for this latter difference lies in that Kreutzer et al.⁴⁹ assumed the liquid film thickness in the slug to be equal to the lubrication film thickness, while the position of the dividing streamline, which separates the liquid film from the recirculating liquid, is actually somewhat more centered. Hence, the diffusion length considered by the correlation is then underestimated.

Finally, an overall mass transfer coefficient is evaluated for H_2 in two distinct ways, either by considering the overall molar flux leaving the bubble surface and transferred to the wall (eq 45) or by considering mass transfer resistances in series and in parallel⁴⁹ (eq 46) and using the coefficients previously calculated by the CFD simulations.

$$[k_L a]_{ov,1} = \frac{\Phi_{caps,H_2} + \Phi_{film,H_2}}{c_{H_2}^* - c_{W,H_2}} \frac{1}{V_{UC}} \quad (45)$$

$$[k_L a]_{ov,2} = k_{GS} a_{GS} + \left(\frac{1}{k_{GL} a_{GL}} + \frac{1}{[k_{LS} a_{LS}]_{H_2}} \right)^{-1} \quad (46)$$

Figure 16 shows the parity diagram for both evaluations at $z = 400$ mm. It is noted that most values remain within the 15% range. This indicates that despite the cross talk phenomenon emphasized previously, the classical representation of mass transfer sequence for the gaseous solute still gives a reliable estimate in the investigated cases.

CONCLUSION AND PROSPECTS

This work focused on the hydrogenation of sunflower oil in a single catalytic channel operating in Taylor flow conditions. The reactor performance was evaluated both experimentally and through CFD simulations to highlight the limiting phenomena.

The CFD model, based on the periodic unit cell approach, included the evolution of oil viscosity and species diffusivity and accounted for both isomerization and successive hydrogenation reactions. Additionally, the bubble shrinkage due to gas consumption was considered by using a moving mesh feature. Numerical simulations could mimic the experimental trends by introducing a corrective factor in the reaction rate expressions to account for catalyst deactivation.

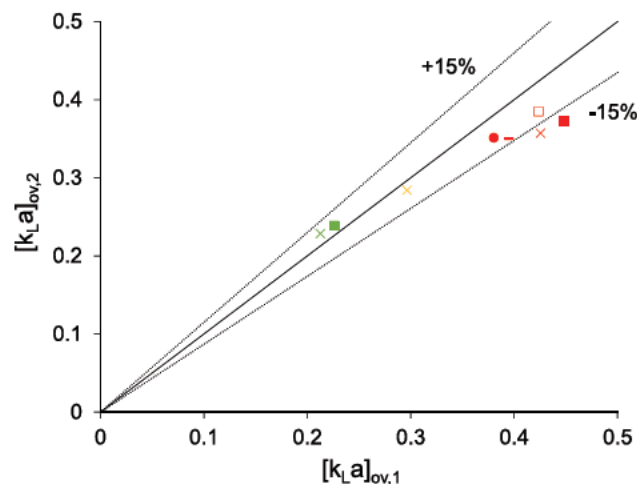


Figure 16. Parity diagram for the overall mass transfer coefficients of H_2 calculated by eqs 45 and 46 at $z = 400$ mm: 80 °C (green), 120 °C (orange), 160 °C (red); $\alpha = 1$ (●), 0.5 (—), 0.2 (×), 0.1 (■); Case 4 (160 °C, 10 bar, $\alpha = 0.1$) (□).

Saturation degrees of the oil obtained from numerical simulations are of the same order of magnitude as those measured (with relative differences between 9% and 19%). Concerning reaction selectivity, the CFD model gives satisfactory results for PUFA and SFA fractions for unsaturation conversion higher than 12%. The *cis* MUFA fraction is correctly predicted, while that of the *trans* counterpart is overestimated for low saturation degree.

Both the experiments and numerical simulations reveal a rather poor selectivity toward the targeted *cis* C18:1 compound with respect to what could be expected from the reaction kinetics. It could be explained by the strong mass transfer resistance of fatty acids (transported as TAG molecules) which tends to consume freshly produced MUFA at the wall. Transport of H_2 also becomes limiting for high catalyst activity or low pressure cases. This depletion of gaseous solute at the catalytic wall then leads to an increased production of *trans* isomers at the expense of their *cis* counterparts.

The same observation arises in all cases when the bubble eventually reaches a critical size where hydrogen transfer through the gas–liquid interface can no longer supply for the reaction. Another consequence of the bubble shrinkage is the reduction of the unit cell velocity along the channel, whose accurate calculation requires updating the bubble surface area.

On the other hand, the mass transfer coefficients inferred from the CFD model are found to be in a good agreement with literature correlations. Moreover, despite exchanges occurring between the lubrication film and the liquid slugs, it is shown that the overall supply of the gaseous reactant to the catalytic wall can be correctly described by a combination of in series and in parallel resistances.

In a future work, the applied moving mesh approach may be extended to two phase flow simulations, which would also allow one to accurately describe the evolution of the bubble shape and lubrication film thickness along the catalytic channel and to extend the model application to much higher bubble velocities (and thus Capillary numbers).

■ ASSOCIATED CONTENT

● Supporting Information

The Supporting Information is available free of charge at <https://pubs.acs.org/doi/10.1021/acs.iecr.1c02801>.

Sunflower oil composition, periodic conditions for hydrodynamics, mesh parameters and sensitivity study, numerical simulations results at $z = 400$ mm, graphical representation of the flow features, and selected boundaries for mass flux evaluation (PDF)

■ AUTHOR INFORMATION

Corresponding Authors

Pierre Albrand – *Laboratoire de Génie Chimique, Université de Toulouse, CNRS, INPT, UPS, Toulouse, France F 31432*;
Phone: +33 (0)5 34 32 37 19; Email: pierre.albrand@toulouse.inp.fr

Carine Julcour – *Laboratoire de Génie Chimique, Université de Toulouse, CNRS, INPT, UPS, Toulouse, France F 31432*;
orcid.org/0000 0002 9364 4862; Phone: +33 (0)5 34 32 37 19; Email: carine.julcour@toulouse.inp.fr

Anne Marie Billet – *Laboratoire de Génie Chimique, Université de Toulouse, CNRS, INPT, UPS, Toulouse, France F 31432*;
Phone: +33 (0)5 34 32 37 19; Email: annemarie.billet@toulouse.inp.fr

Complete contact information is available at: <https://pubs.acs.org/doi/10.1021/acs.iecr.1c02801>

Notes

The authors declare no competing financial interest.

■ ACKNOWLEDGMENTS

The authors are grateful to Jean Louis Labat and Lahcen Farhi from the technical team of *Laboratoire de Génie Chimique* for assembling the pilot unit and later on adapting it for edible oil hydrogenation. They also thank Caroline Dubois from COMSOL France (Grenoble, France) and her colleagues for their help concerning the moving mesh approach. Finally, they thank Guillaume Chollet from *Institut des Corps Gras* (ITERG, Pessac, France) for constructive discussions.

■ NOMENCLATURE

Acronyms

ALE = arbitrary Lagrangian Eulerian
CFD = computational fluid dynamics
MUFA = monounsaturated fatty acids (here C18:1)
PUFA = polyunsaturated fatty acids (here C18:2)
SFA = saturated fatty acids (here C18:0)
TAG = triacylglycerol
TFA = *trans* fatty acids
UC = unit cell

Symbols

A = constant for $D_{TAG-oil}$ (see eq 12), SI
 a_{GL} = bubble interfacial area at the caps (see eq 42), ($m_B^2 \cdot m_{UC}^{-3}$)
 a_{GS} = bubble interfacial area at the lubrication film (see eq 41), ($m_B^2 \cdot m_{UC}^{-3}$)
 a_{LS} = wall interfacial area (see eqs 43 and 44), ($m_W^2 \cdot m_{UC}^{-3}$)
 c_i = concentration of component i , ($mol\ m_L^{-3}$)
 $c_{L,i}$ = volume averaged concentration of component i , as defined in eq 34, ($mol\ m_L^{-3}$)
 $c_{W,i}$ = wall surface averaged concentration of component i , as defined in eq 35, ($mol\ m_L^{-3}$)
 $c_{H_2}^*$ = dissolved hydrogen concentration at saturation (see eq 30), ($mol\ m_L^{-3}$)
 d_C = channel diameter, (m)
 d_B = bubble diameter, (m)
 dS_B = elementary bubble surface, (m_B^2)
 dS_W = elementary wall surface, (m_W^2)
 $D_{TAG-oil}$ = triacylglycerol diffusivity in oil, ($m^2\ s^{-1}$)
 D_{H_2-oil} = hydrogen diffusivity in oil, ($m^2\ s^{-1}$)
 dV = elementary volume, (m^3)
 g = gravity vector, ($m\ s^{-2}$)
 H_0 = pre exponential factor for Henry's constant (see eq 30), ($mol\ m^{-3}\ Pa^{-1}$)
 k_{GL} = gas–liquid mass transfer coefficient, ($m\ s^{-1}$)
 $k_{GL}a_{GL}$ = volumetric gas–liquid mass transfer coefficient, (s^{-1})
 $k_{GS}a_{GS}$ = volumetric gas–solid mass transfer coefficient, (s^{-1})
 $k_{LS}a_{LS}$ = volumetric liquid–solid mass transfer coefficient, (s^{-1})
 K_{iso} = *trans* over *cis* MUFA equilibrium constant, (–)
 L_f = lubrication film length, (m)
 L_S = liquid slug length, (m)
 L_{UC} = unit cell length, (m)
 M_{oil} = molar mass of the oil, ($g\ mol^{-1}$)
 n_1 = power exponent for the viscosity in eq 11 (expression of H_2 diffusivity in oil), (–)
 n_2 = power exponent for the viscosity in eq 12 (expression of TAG diffusivity in oil), (–)
 p' = average number of insaturations per fatty acid in a given oil, (–)
 P_{H_2} = hydrogen pressure, (Pa)
 P = total pressure, (Pa)
 R = universal gas constant, ($J\ mol^{-1}\ K^{-1}$)
 R_B = bubble radius, (m)
 R_C = channel radius, (m)
 r_i = algebraic production rate of species i as defined through eqs 13–eq 17, ($mol\ kg_{pd}^{-1}\ s^{-1}$)
 T = temperature, (K)
 t = time, (s)
 u = velocity vector, ($m\ s^{-1}$)
 U_B = bubble velocity, ($m\ s^{-1}$)

u_{GS} = gas superficial velocity, (m s^{-1})
 u_{LS} = liquid superficial velocity, (m s^{-1})
 U_{TP} = two phase velocity, $U_{TP} = u_{GS} + u_{LS}$, (m s^{-1})
 V_{H_2} = molar volume of hydrogen at its bubble point, ($\text{m}^3 \text{ kmol}^{-1}$)
 V_B = bubble volume, (m^3)
 V_L = liquid volume, (m^3)
 V_{UC} = unit cell volume, (m^3)
 w_{Pd} = palladium mass fraction within the washcoat, (–)
 X = saturation degree, as defined in eq 2, (–)
 x_L = PUFA molar fraction, (–)
 x_C = *cis* MUFA molar fraction, (–)
 x_T = *trans* MUFA molar fraction, (–)
 x_S = SFA molar fraction, (–)
 z = axial position of the UC along the channel, (m)

Greek Symbols

α = apparent catalyst activity ($0 < \alpha \leq 1$), (–)
 δ_c = washcoat thickness, (m)
 δ_f = lubrication film thickness, (m)
 ΔE = heat of absorption (see eq 30), ($\text{J} \cdot \text{mol}^{-1}$)
 ϵ_G = gas holdup, (–)
 κ_1 = kinetic constant of MUFA hydrogenation rate, ($\text{mol kg}_{Pd}^{-1} \text{ s}^{-1}$)
 κ_2 = kinetic constant of PUFA hydrogenation rate, ($\text{mol kg}_{Pd}^{-1} \text{ s}^{-1}$)
 κ_{iso} = kinetic constant of *cis* MUFA to *trans* MUFA isomerization, ($\text{mol kg}_{Pd}^{-1} \text{ s}^{-1}$)
 μ_L = liquid dynamic viscosity, (Pa s)
 ϕ = ratio of $r_{2,C}$ over $r_{2,T}$, (–)
 $\phi_{W,i}$ = local molar flux at the channel wall for a given species i , ($\text{mol m}^{-2} \text{ s}^{-1}$)
 Φ_{W,FA_i} = overall molar flux at the channel wall for a given fatty acid i , (mol s^{-1})
 Φ_{B,H_2} = overall molar flux at the gas–liquid interface for H_2 , (mol s^{-1})
 ρ_L = liquid density, (kg m^{-3})
 ρ_S = apparent washcoat density, (kg m^{-3})
 σ_L = liquid surface tension, (N m^{-1})
 Θ = solvent association parameter as defined in eq 11 (–)
 θ_i = fractional surface coverage of species i (fatty acid or H_2) on the catalyst surface (expressed as a function of the liquid phase concentrations assuming adsorption equilibrium), (–)

Dimensionless Groups

Ca = Capillary number, $\frac{\mu_L U_B}{\sigma_L}$, (–)
 Bo = Bond number, $(\rho_L - \rho_G) g d_c^2 / \sigma_L$, (–)
 Pe_i = Péclet number, $\frac{(U_{TP} - 1 / 2 U_B) d_c^2}{L_S D_{i-oil}}$, (–)
 Re = Reynolds number, $\frac{\rho_L U_B d_c}{\mu_L}$, (–)
 Re_{TP} = Two phase flow Reynolds number, $\frac{\rho_L U_{TP} d_c}{\mu_L}$, (–)
 Re_L = Reynolds number of the liquid phase, $\frac{\rho_L u_{LS} d_c}{\mu_L}$, (–)
 Sc_i = Liquid Schmidt number for TAG, $\frac{\mu_L}{\rho_L D_{i-oil}}$, (–)
 We = Weber number, $\rho_L U_B^2 d_c / \sigma_L$, (–)

Subscript

0 = at the channel inlet
 L = liquid in the unit cell
 B = bubble
 UC = unit cell
 W = wall

REFERENCES

- (1) Kellens, M.; Calliauw, G. Oil Modification Processes. In *Edible Oil Processing*, 2nd ed.; Calliauw, G., Hamilton, R. J., Hamm, W., Eds.; John Wiley & Sons, Inc., 2013; Chapter 6.
- (2) Cap, D. S. Cosmetic product including vegetable oil blend. U.S. Patent USUS8709453B2 2014.
- (3) Mozaffarian, D.; Aro, A.; Willett, W. C. Health effects of trans fatty acids: experimental and observational evidence. *Eur. J. Clin. Nutr.* **2009**, *63*, S5–S21.
- (4) Clarke, R.; Frost, C.; Collins, R.; Appleby, P.; Peto, R. Dietary lipids and blood cholesterol: quantitative meta analysis of metabolic ward studies. *BMJ.* **1997**, *314*, 112–112.
- (5) Faur, L. In *Oils & Fats Manual*; Publishing, L., Ed.; 1992.
- (6) Belkacemi, K.; Boulmerka, A.; Arul, J.; Hamoudi, S. Hydrogenation of Vegetable Oils with Minimum trans and Saturated Fatty Acid Formation Over a New Generation of Pd catalyst. *Top. Catal.* **2006**, *37*, 113–120.
- (7) Veldsink, J. W.; Bouma, M. J.; Schöön, N. H.; Beenackers, A. A. Heterogeneous hydrogenation of vegetable oils: a literature review. *Catal. Rev.: Sci. Eng.* **1997**, *39*, 253–318.
- (8) Veldsink, J. W. Selective hydrogenation of sunflower seed oil in a three phase catalytic membrane reactor. *J. Am. Oil Chem. Soc.* **2001**, *78*, 443–446.
- (9) Fritsch, D.; Bengtson, G. Development of catalytically reactive porous membranes for the selective hydrogenation of sunflower oil. *Catal. Today* **2006**, *118*, 121–127.
- (10) Macher, M. B.; Högberg, J.; Möller, P.; Härröd, M. Partial hydrogenation of fatty acid methyl esters at supercritical conditions. *European Journal of Lipid Science and Technology* **1999**, *101*, 301–305.
- (11) Boger, T.; Zieverink, M. M.; Kreutzer, M. T.; Kapteijn, F.; Moulijn, J. A.; Addiego, W. P. Monolithic catalysts as an alternative to slurry systems: hydrogenation of edible oil. *Ind. Eng. Chem. Res.* **2004**, *43*, 2337–2344.
- (12) Boldrini, D. E.; Sanchez M., J. F.; Tonetto, G. M.; Damiani, D. E. Monolithic Stirrer Reactor: Performance in the Partial Hydrogenation of Sunflower Oil. *Ind. Eng. Chem. Res.* **2012**, *51*, 12222–12232.
- (13) Durán Martínez, F. Réacteur échangeur de type monolith stratégie de modélisation et description des phénomènes à l'échelle d'un canal catalytique unique. Ph.D. thesis, *Toulouse INP*, 2017.
- (14) Woo, M.; Deutschmann, O.; Wörner, M. Influence of liquid composition on diffusive mass transfer in the lubricating film of Taylor flow—A study related to the hydrogenation of nitrobenzene. *Chem. Eng. Process.* **2020**, *149*, 107835.
- (15) Woo, M.; Tischer, S.; Deutschmann, O.; Wörner, M. A step toward the numerical simulation of catalytic hydrogenation of nitrobenzene in Taylor flow at practical conditions. *Chem. Eng. Sci.* **2021**, *230*, 116132.
- (16) *Structured Catalysts and Reactors*; Cybulski, A., Moulijn, J. A., Eds.; CRC Press, 2005.
- (17) Angeli, P.; Gavrilidis, A. Hydrodynamics of Taylor flow in small channels: A Review. *Proc. Inst. Mech. Eng., Part C* **2008**, *222*, 737–751.
- (18) Shao, N.; Gavrilidis, A.; Angeli, P. Flow regimes for adiabatic gas–liquid flow in microchannels. *Chem. Eng. Sci.* **2009**, *64*, 2749–2761.
- (19) Talimi, V.; Muzychka, Y.; Kocabiyik, S. A review on numerical studies of slug flow hydrodynamics and heat transfer in microtubes and microchannels. *Int. J. Multiphase Flow* **2012**, *39*, 88–104.
- (20) Suo, M.; Griffith, P. Two Phase Flow in Capillary Tubes. *J. Basic Eng.* **1964**, *86*, 576–582.
- (21) Brauner, N.; Maron, D. M. Identification of the range of 'small diameters' conduits, regarding two phase flow pattern transitions. *Int. Commun. Heat Mass Transfer* **1992**, *19*, 29–39.
- (22) Etmnan, A.; Muzychka, Y. S.; Pope, K. A Review on the Hydrodynamics of Taylor Flow in Microchannels: Experimental and Computational Studies. *Processes* **2021**, *9*, 870.
- (23) Albrand, P.; Julcour, C.; Gerbaud, V.; Billet, A. M. Accurate hydrogenated vegetable oil viscosity predictions for monolith reactor simulations. *Chem. Eng. Sci.* **2020**, *214*, 115388.

- (24) Albrand, P.; Julcour, C.; Veyrine, F.; Billet, A. M. Sunflower oil hydrogenation mechanisms and kinetics. *Chem. Eng. J.* **2021**, *420*, 129854.
- (25) Zhou, Y.; Al Dahhan, M.; Dudukovic, M.; Liu, H. Effect of Distributor Design on Gas Liquid Distribution in Monolithic Bed at High Gas/Liquid Ratios. *Chin. J. Chem. Eng.* **2012**, *20*, 693–700.
- (26) Devatine, A.; Chaumat, H.; Guillaume, S.; Tati Tchibouanga, B.; Duran Martinez, F.; Julcour, C.; Billet, A. M. Hydrodynamic study of a monolith type reactor for intensification of gas liquid applications. *Chem. Eng. Process.* **2017**, *122*, 277–287.
- (27) Yang, C. Y.; Shieh, C. C. Flow pattern of air–water and two phase R 134a in small circular tubes. *Int. J. Multiphase Flow* **2001**, *27*, 1163–1177.
- (28) Giavedoni, M. D.; Saita, F. A. The rear meniscus of a long bubble steadily displacing a Newtonian liquid in a capillary tube. *Phys. Fluids* **1999**, *11*, 786–794.
- (29) Fukagata, K.; Kasagi, N.; Ua arayaporn, P.; Himeno, T. Numerical simulation of gas–liquid two phase flow and convective heat transfer in a micro tube. *Int. J. Heat Fluid Flow* **2007**, *28*, 72–82.
- (30) Gupta, R.; Fletcher, D.; Haynes, B. Taylor Flow in Micro channels: A Review of Experimental and Computational Work. *J. Comput. Multiphase Flows* **2010**, *2*, 1–31.
- (31) Bretherton, F. P. The motion of long bubbles in tubes. *J. Fluid Mech.* **1961**, *10*, 166–188.
- (32) Haase, S.; Murzin, D. Y.; Salmi, T. Review on hydrodynamics and mass transfer in minichannel wall reactors with gas–liquid Taylor flow. *Chem. Eng. Res. Des.* **2016**, *113*, 304–329.
- (33) Durán Martínez, F.; Julcour, C.; Billet, A. M.; Larachi, F. Modelling and simulations of a monolith reactor for three phase hydrogenation reactions — Rules and recommendations for mass transfer analysis. *Catal. Today* **2016**, *273*, 121–130.
- (34) Aussillous, P.; Quéré, D. Quick deposition of a fluid on the wall of a tube. *Phys. Fluids* **2000**, *12*, 2367.
- (35) van Baten, J.; Krishna, R. CFD simulations of mass transfer from Taylor bubbles rising in circular capillaries. *Chem. Eng. Sci.* **2004**, *59*, 2535–2545.
- (36) Ceriani, R.; Meirelles, A. J. Predicting vapor–liquid equilibria of fatty systems. *Fluid Phase Equilib.* **2004**, *215*, 227–236.
- (37) Bartsch, A. Beschleunigung des Stoffaustausches von Gas Flüssigkeits Reaktionen durch Schallwellen am Beispiel der Fetthärtung. *Z. Naturforsch., A: Phys. Sci.* **1995**, *50*, 228–234.
- (38) Topallar, H.; Bayrak, Y.; Iscan, M. Effect of hydrogenation on density and viscosity of sunflowerseed oil. *J. Am. Oil Chem. Soc.* **1995**, *72*, 1519–1522.
- (39) Noh, W. F. *CEL: A time dependent, two space dimensional, coupled Eulerian Lagrange code*; U.S. Department of Energy, 1963.
- (40) Hirt, C.; Amsden, A.; Cook, J. An arbitrary Lagrangian Eulerian computing method for all flow speeds. *J. Comput. Phys.* **1974**, *14*, 227–253.
- (41) Hughes, T. J.; Liu, W. K.; Zimmermann, T. K. Lagrangian Eulerian finite element formulation for incompressible viscous flows. *Computer Methods in Applied Mechanics and Engineering* **1981**, *29*, 329–349.
- (42) Fillion, B.; Morsi, B. I.; Heier, K. R.; Machado, R. M. Kinetics, Gas Liquid Mass Transfer, and Modeling of the Soybean Oil Hydrogenation Process. *Ind. Eng. Chem. Res.* **2002**, *41*, 697–709.
- (43) Taylor, G. I. Deposition of a viscous fluid on the wall of a tube. *J. Fluid Mech.* **1961**, *10*, 161.
- (44) Thulasidas, T.; Abraham, M.; Cerro, R. Flow patterns in liquid slugs during bubble train flow inside capillaries. *Chem. Eng. Sci.* **1997**, *52*, 2947–2962.
- (45) Yang, L.; Nieves Remacha, M. J.; Jensen, K. F. Simulations and analysis of multiphase transport and reaction in segmented flow microreactors. *Chem. Eng. Sci.* **2017**, *169*, 106–116.
- (46) Nirmal, G. M.; Leary, T. F.; Ramachandran, A. Mass transfer dynamics in the dissolution of Taylor bubbles. *Soft Matter* **2019**, *15*, 2746–2756.
- (47) Butler, C.; Cid, E.; Billet, A. M.; Lalanne, B. Numerical simulation of mass transfer dynamics in Taylor flows. *Int. J. Heat Mass Transfer* **2021**, *179*, 121670.
- (48) Hatziantoniou, V.; Andersson, B. Solid liquid mass transfer in segmented gas liquid flow through a capillary. *Ind. Eng. Chem. Fundam.* **1982**, *21*, 451–456.
- (49) Kreutzer, M. T.; Du, P.; Heiszwolf, J. J.; Kapteijn, F.; Moulijn, J. A. Mass transfer characteristics of three phase monolith reactors. *Chem. Eng. Sci.* **2001**, *56*, 6015–6023.

SUPPORTING INFORMATION

Sunflower hydrogenation in Taylor flow conditions: experiments and CFD modelling using moving mesh approach

Pierre Albrand,* Carine Julcour,* and Anne-Marie Billet*

*Laboratoire de Génie Chimique, Université de Toulouse, CNRS, INPT, UPS, Toulouse,
France*

E-mail: pierre.albrand@toulouse-inp.fr; carine.julcour@toulouse-inp.fr;

annemarie.billet@toulouse-inp.fr

Phone: +33 (0)5 34 32 37 19

Edible oil composition

The sunflower oil composition before hydrogenation is available in Tab. S1.

Table S1: Composition of sunflower oil before hydrogenation

	Fatty acid [†]	Molar fraction (-%)
	C14:0	0.07
	C16:0	5.93
<i>cis</i>	C16:1	0.09
<i>trans</i>	C16:1	-
	C17:0	0.04
<i>cis</i>	C17:1	-
	C18:0	3.83
<i>cis</i>	C18:1	29.92
<i>trans</i>	C18:1	0.01
<i>cis</i>	C18:2	58.54
<i>trans</i>	C18:2	0.02
<i>cis</i>	C18:3	0.12
<i>trans</i>	C18:3	0.06
	C20:0	0.27
<i>cis</i>	C20:1	0.14
<i>trans</i>	C20:1	-
	C22:0	0.73
<i>cis</i>	C22:1	-
<i>trans</i>	C22:1	-
	C24:0	0.24
<i>cis</i>	C24:1	-

[†] In CX:Y notation, X stands for the number of carbons in the fatty acid chain, and Y the number of unsaturations in this chain.

Periodic conditions for hydrodynamics

As stated in the main text, mass conservation issues were observed when moving mesh and the by-default periodic conditions between the top and bottom of the UC were applied for hydrodynamics. This inconsistency seems to be related to the fact that the moving boundaries at the UC ends here differ from walls, since they exhibit a non-zero mass transfer flux.

Subsequently, periodic condition were set manually for the hydrodynamics to account

for the mesh displacement related to the ALE method. An outlet flow condition was set at the bottom of the UC. At the top of the UC, the velocity profile was calculated thanks to a COMSOL built-in coupling variable (general extrusion operator) according to Eq. (S1).

$$u(r)|_{Top,flow} = \left(u(r)|_{Bottom,flow} - u|_{Bottom,mesh} \right) + u|_{Top,mesh} \quad (S1)$$

Mesh parameters and sensitivity study

Maximal element sizes were defined at the wall and gas-liquid interface (l_{wall}), as well as within free mesh subdomains #1, #3, #5 and #7 (l_{domain}). Conversely, axial and radial element distributions (n_z and n_r) were given for mapped mesh in subdomains #2, #4 and #6.

Tab. S2 compares the saturation degree X obtained at the reactor outlet (after a channel length of 400 mm) for three different meshing configurations, where N_{total} is the total mesh number.

Table S2: Mesh sensitivity analysis for the 160°C - 21 bar, case with $\alpha = 1$

Case	l_{domain} (μm)	l_{wall} (μm)	$n_{r,slug}$ (-)	$n_{z,slug}$ (-)	$n_{r,film}$ (-)	$n_{z,film}$ (-)	N_{total} (-)	X ($z = 400$ mm) (%)
#M1	15	5	100	150	15	1,200	167,722	13.30
#M2	20	7.5	75	100	10	900	94,230	13.32
#M3	25	10	50	75	7	700	58,298	13.42

While the total cell number of #M1 is about 3 times higher than that of #M3, it results in a relative difference of less than 1% for X . This difference drops to 0.2% between #M1 and #M2 with a 43% difference in the cell number. Thus, #M1 meshing corresponds to a convergence plateau regarding X values. It has been applied for all subsequent calculations (whose results are shown in the paper).

Fig. S1 shows the radial normalized concentration profiles of the different species at half slug and half film for $z = 400$ mm (Case 1a - $L_{UC} = 40$ mm - $\alpha = 1$) and the corresponding

mesh position. Even though, rather sharp gradients are observed for the fatty acids near the catalytic wall at half slug (see Fig. S1a for $r \rightarrow 1$ mm), concentration profiles are correctly described, which supports the fact that an adequate mesh grid was applied. Additionally, it is recalled that a third order polynomial interpolation scheme is considered for mass transport which increased the resolution already provided by the mesh.

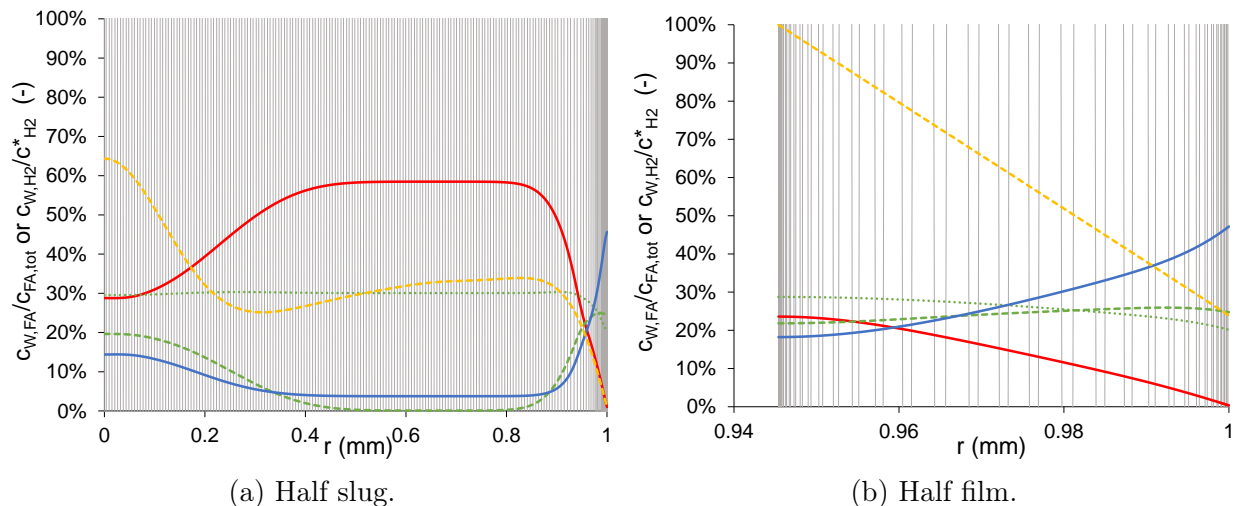


Figure S1: Radial normalized concentrations of fatty acids and H_2 at half slug and half film for Case 1a (160°C - 21 bar - $L_{UC,0} = 40$ mm) for $\alpha = 1$: C18:2 (red —), *cis* C18:1 (green \cdots), *trans* C18:1 (green - -), C18:0 (blue —), H_2 (yellow - -), mesh radial position (grey grid).

Finally, mesh quality eventually deteriorates due to the displacement of the boundaries. A mesh distortion parameter - defined as the first invariant of the isochoric Green–Lagrange strain - is calculated to prevent such phenomenon. Here, calculation was stopped when this variable exceeded 3.5.

Numerical results at $z = 400$ mm

Tab. S3 shows all the simulation results at $z = 400$ mm. It is noted that twice shorter $L_{UC,0}$ induces 5.6% higher conversion (see Case 1b compared to Case 1a - $\alpha = 0.2$). The effect of $L_{UC,0}$ on hydrogenated oil composition is also limited: it yields a slight increase in *cis* MUFA, *trans* MUFA and SFA fractions and a minor decrease in PUFA fraction.

Table S3: Numerical simulations results at $z = 400$ mm

Associated experiments	Case	α (-)	$t_{p,z=400}$ mm (s)	x_L (%-mol)	x_C (%-mol)	x_T (%-mol)	x_S (%-mol)	X (%)
MT1-C1, MT1-C2, MT2-C3-A1, and MT2-C3-A4	1a	1	8.8	45.1	29.3	8.1	9.9	13.3
		0.5	8.7	45.0	30.3	8.9	8.2	12.2
		0.2	8.4	45.3	31.9	9.2	6.0	10.6
		0.1	8.1	46.1	33.2	8.2	4.9	9.3
<i>Idem</i> to Case 1a	1b	0.2	8.5	44.5	32.1	9.6	6.2	11.2
MT2-C3-A2	2	0.2	14.0	47.0	31.8	7.1	6.5	9.7
MT2-C3-A3	3	0.2	26.0	47.5	31.7	5.5	7.8	10.2
		0.1	25.0	48.6	33.6	4.6	5.7	8.1
MT2-C3-A5	4	0.1	7.7	49.8	31.7	6.9	4.0	6.1

Graphical representation of the flow features and selected boundaries for mass flux evaluation

Fig. S2 shows the dividing streamline and the associated stagnation points near the bubble rear. Furthermore, the selected boundaries used to estimate interphase mass fluxes are shown around the bubble nose.

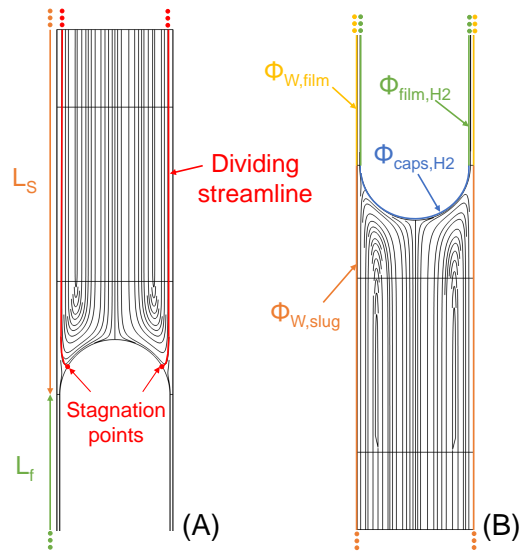


Figure S2: Dividing streamline representation at the bubble tail (A) and selected boundaries for mass fluxes calculated at the bubble nose (B) (Case 1a, catalytic section inlet).